nature neuroscience

ARTICLES

https://doi.org/10.1038/s41593-022-01027-3

Gut microbiota drives age-related oxidative stress and mitochondrial damage in microglia via the metabolite N^6-carboxymethyllysine

Omar Mossad[1,2], Bérénice Batut[3], Bahtiyar Yilmaz[4], Nikolaos Dokalis[1,2], Charlotte Mezö[1,2], Elisa Nent[5], Lara Susann Nabavi[1], Melanie Mayer[1], Feres José Mocayar Maron[1], Joerg M. Buescher[5], Mercedes Gomez de Agüero[4], Antal Szalay[6], Tim Lämmermann[5], Andrew J. Macpherson[4], Stephanie C. Ganal-Vonarburg[4], Rolf Backofen[3,7], Daniel Erny[1,8], Marco Prinz[1,9,10] and Thomas Blank[1]✉

Microglial function declines during aging. The interaction of microglia with the gut microbiota has been well characterized during development and adulthood but not in aging. Here, we compared microglial transcriptomes from young-adult and aged mice housed under germ-free and specific pathogen-free conditions and found that the microbiota influenced aging associated-changes in microglial gene expression. The absence of gut microbiota diminished oxidative stress and ameliorated mitochondrial dysfunction in microglia from the brains of aged mice. Unbiased metabolomic analyses of serum and brain tissue revealed the accumulation of N^6-carboxymethyllysine (CML) in the microglia of the aging brain. CML mediated a burst of reactive oxygen species and impeded mitochondrial activity and ATP reservoirs in microglia. We validated the age-dependent rise in CML levels in the sera and brains of humans. Finally, a microbiota-dependent increase in intestinal permeability in aged mice mediated the elevated levels of CML. This study adds insight into how specific features of microglia from aged mice are regulated by the gut microbiota.

In recent years, microglia have been extensively studied in physiological and pathological brain aging[1]. During normal brain aging, microglia display a distinct transcriptional profile that, in many ways, strides toward neurodegeneration[2]. At the same time, microglia in the aged human brain have been defined as dystrophic; this is characterized by morphological changes and reduced tissue support[3]. Age-related changes in microglia homeostasis are not solely intrinsic but are also mediated through bidirectional interaction between the CNS and the peripheral environment. The importance of such a link is increasingly recognized and seems to be mediated by various systemic factors, such as the gut microbiota, which signals along the microbiota–gut–brain axis[4]. The gut microbiota is a key mediator in the communication between the gut and the brain by regulating microglial function and maturation[5–7]. A dysregulation of this communication may be critical in mediating age-related decline in microglial physiology[8,9]. An important point in this context is the substantial change in the composition of the intestinal microbiota with aging in humans[10,11] and mice[12]. These age-related changes might shift the microbial metabolome or alter intestinal permeability, which would increase the blood concentrations of gut-derived metabolites. Indeed, heterochronic microbiota transplantation in mice has been shown to reverse age-related cognitive decline[13,14], with alterations in expression of microglial genes in the hippocampus[13]. While metabolites from the gut are known to reach the brain[15], their specific influence on microglial aging is elusive.

In this study, we describe a cross-sectional framework for the communication between the gut microbiota and the brain in young-adult and aged mice. Specific transcriptional profiles provide new insights into how the gut microbiota influences the homeostasis of microglia in the aging brain. Molecular phenotyping at the metabolite level identified CML, a major advanced glycation end product (AGE), as a key compound responsible for age-related microglial dysfunction.

Results

The gut microbiota alters the microglial transcriptomic profile in aging. A higher microglial cell density was reported with aging in the brain cortex[16]. We confirmed the increased microglial cell density in the cortex of specific pathogen-free (SPF) and germ-free (GF) animals between young-adult and aged mice (Extended Data Fig. 1a,b) but found no difference between aged SPF and GF mice (Extended Data Fig. 1a,b). One of the most prominent and first identified features of aging microglia is their change in morphology[3]. These morphological alterations include cytoplasmic beading formation and shortened processes. To determine the potential morphological changes in microglia of SPF and

[1]Institute of Neuropathology, Faculty of Medicine, University of Freiburg, Freiburg, Germany. [2]Faculty of Biology, University of Freiburg, Freiburg, Germany. [3]Bioinformatics Group, Department of Computer Science, University of Freiburg, Freiburg, Germany. [4]Maurice Müller Laboratories, Department for Biomedical Research, University Clinic of Visceral Surgery and Medicine, Inselspital, University of Bern, Bern, Switzerland. [5]Max Planck Institute of Immunobiology and Epigenetics, Freiburg, Germany. [6]Ultimate Medicine AG, Dübendorf, Switzerland. [7]Centre for Integrative Biological Signalling Studies, University of Freiburg, Freiburg, Germany. [8]Berta Ottenstein Program, Faculty of Medicine, University of Freiburg, Freiburg, Germany. [9]Center for NeuroModulation, Faculty of Medicine, University of Freiburg, Freiburg, Germany. [10]Signalling Research Centers BIOSS and CIBSS, University of Freiburg, Freiburg, Germany.
✉e-mail: thomas.blank@uniklinik-freiburg.de

GF mice, we performed quantitative morphometric reconstruction. The microglia of SPF mice displayed a notable reduction in total branch area, total branch length and the number of branch points, together with an increase in cell body volume (Extended Data Fig. 1c–g). Cell body sphericity was not altered between the groups (Extended Data Fig. 1h). From these data, it was evident that age had a profound effect on microglial morphology in SPF mice while microglia were unaltered and hyper-ramified under GF conditions.

To further evaluate the microbiota-dependent alterations of microglial physiology in the aging brain, we performed RNA sequencing (RNA-seq) on fluorescence-activated cell sorting (FACS)-purified microglia (Extended Data Figs. 2a and 3a) from the whole brains of young-adult (6–10-week-old) and aged (96–104-week-old) male and female mice, housed under GF or SPF conditions (Fig. 1a, Extended Data Fig. 3b and Supplementary Tables 1–3). Principal component analysis (PCA) highlighted distinct gene expression profiles of microglia in GF and SPF mice across both age groups (Fig. 1b). Interestingly, the transcriptomic differences between microglia isolated from GF and SPF mice were more prominent at older ages (Fig. 1c). Remarkably, when compared to microglia from SPF mice, an age-independent gene expression pattern emerged in the microglia of GF mice (microglial GF signature), which included genes related to the cytoskeleton (for example, *Sdc3*, *Sult1a1* and *Tuba4a*) and immune function (for example, *Ctse*, *Ero1lb*, *Htra3*, *Kcnma1*, *Notch4*, *Nr1d2*, *Rab4a* and *Wdfy1*) (Fig. 1d and Supplementary Table 4). Moreover, the microglial GF signature contained genes associated with the regulation of mitochondrial function (for example, *B4galnt1*, *Gpr137b*, *Gstm1*, *Mcur1*, *Mtfp1*, *Nnt* and *Plcd3*), which suggests a capacity of the microbiota to regulate the metabolic profile of microglia (Fig. 1d and Supplementary Table 4). Next, we characterized the functional changes in gene expression in microglia with regard to age and microbiota using a weighted gene coexpression network analysis (WGCNA)[17] (Fig. 1e,f and Extended Data Fig. 3c). Genes that significantly (Wald $P_{adj} < 0.05$) explained more than 50% of the variance were binned into module eigengenes (MEs) based on their coexpression pattern. In line with previous reports[18], on comparing the young-adult groups under SPF or GF housing, we observed minor differences in the gene networks associated with immune function and epigenetic regulation—ME1, ME5, ME6 and ME7, respectively. Two modules stood out in each age group. ME1 and ME4 in the aged SPF group included genes related to processes like mitochondrial metabolism and lipid localization, while ME2 and ME6 in the aged GF group included genes that regulate the immune response, histone lysine methylation and cell morphogenesis (Extended Data Fig. 3d).

We next examined the microbiota's contribution to the age-related MEs. WGCNA revealed that microglia from aged GF mice followed the general aging trend in SPF mice, but with lower magnitude (Fig. 1e,f), and clustered closer to the young-adult groups (Extended Data Fig. 3b). For example, genes in ME1 and ME8 associated with immune response (for example, *Axl*, *Crlf2*, *Tnfsf8*, *Tnfsf10*, *Ccl12*, *Fgr*, *Il1b*, *Il6st*, *Spp1* and *Tlr2*), interferon signaling (for example, *Cxcl10*/*8*, *Ifi207*, *Ifit2*/*8* and *Stat1*), inflammatory response (for example, *Cd180*, *Ldlr*, *S100a8* and *S100a9*) and microglial cell migration (for example, *Ccl12* and *Cxcl10*) showed a specific upregulation in the microglia of aged SPF mice, while having negative or low correlation in both young-adult groups and aged GF mice (Fig. 2a and Extended Data Fig. 3c,d). Microglia showed evident alterations in their transcriptomic profile with aging, with striking microbiota-dependent divergences.

Reduced oxidative stress in the microglia of aged GF mice. A key feature of cellular aging in microglia is increased oxidative stress, which refers to elevated intracellular levels of reactive oxygen species (ROS)[19]. In fact, on inspecting the pathways in the age-related modules, we found several connections to the regulation of oxidative stress in microglia that were dependent on the microbiota. Notably, ME1 and ME8 showed a strong correlation in the aged SPF group, including mitochondrial metabolic processes, hydrogen peroxide metabolic processes and ROS metabolic processes. ME2, which was highly enriched in aged GF mice, was associated with response to oxygen-containing compounds (Figs. 1e,f and 2a). To confirm that the expression levels of microglial ROS-related genes were regulated by the age of the mice and housing condition, we selectively analyzed ROS-related genes in the age-related ME1, ME2 and ME8 (Fig. 2b). As hypothesized, we found a specific upregulation of several immune activation and ROS-promoting genes, such as *Cdkn1a*, *Cyba*, *Cybb*, *Duoxa1*, *Il1b*, *Tgfbr2*, *Tlr2*, *Tlr4* and *Tlr5*, and ROS response genes, such as *Axl*, *Hif1a*, *Lcn2*, *Mmp2*, *Rela*, *Trex1*, *S100a8* and *S100a9*, only in the microglia of aged SPF mice (Fig. 2b). Genes in ME2, which included genes that regulate cellular ROS levels, such as *Foxp1*, *Nrf1* and *Trp53*, and genes implicated in the regulation of mitochondrial ROS, such as *G6pdx*, *Pdk2*, *Stat3* and *Ucp2*, were less expressed in the microglia of aged SPF mice compared to age-matched GF mice (Fig. 2b). In addition to addressing the expression of ROS-related genes, we monitored ROS production in the microglia isolated from young-adult and aged SPF mice using the CellROX flow cytometry assay and found a significant elevation of ROS with increasing age, which was greatly reduced in aged GF mice (Fig. 2c). Activation of inducible nitric oxide synthase (iNOS) is directly linked to the generation of excessive ROS[20,21]. Using immunohistochemistry (IHC), we observed an age-dependent increase in microglial iNOS expression under SPF conditions, but this increase was less pronounced in GF mice (Fig. 2d,e).

Next, we aimed to investigate how the increase in ROS might affect microglial function. Despite the lack of agreement on cause and effect, the accumulation of ROS in the aging brain is associated with mitochondrial damage and mitochondrial dysfunction[22]. Indeed, in ME3, ME5 and ME9, we found prominent changes in genes related to mitochondrial assembly, carbohydrate metabolism and oxidative phosphorylation (Fig. 2f). Electron microscopy examination of microglial mitochondria revealed a substantially higher percentage of damaged mitochondria with less well-defined or even destroyed cristae in aged SPF mice relative to aged GF mice, with no change in mitochondrial mass or number per microglia (Fig. 2g,h and Extended Data Fig. 4a–c). Furthermore, the accumulation of cellular ROS, which peaked in the microglia of aged SPF mice, can induce the expression of hypoxia inducible factor 1 subunit Alpha (*Hif1a*). HIF1a is linked to ROS in pseudo-hypoxic states in the brain and can directly alter mitochondrial metabolism[23]. Mitochondrial dysfunction in the aged brain leads to a metabolic shift, which is associated with the exaggerated activation of microglia. Indeed, while young-adult mice showed similar *Hif1a* expression, RNA-seq and quantitative PCR with reverse transcription (RT–qPCR) indicated higher *Hif1a* expression in the microglia from aged SPF mice than GF mice (Extended Data Fig. 4d,e). The efficiency of oxidative phosphorylation declines in cells of aged animals and leads to reduced ATP production[24]. The transmembrane potential ($\Delta\psi m$) of mitochondria is the major driver of ATP production. To account for an increase in mitochondrial mass with age (Extended Data Fig. 4f,g), we plotted mitochondrial activity as the transmembrane potential of mitochondria relative to the mitochondrial mass. The mitochondrial activity showed an age-associated drop and a reduction in the intracellular ATP reservoir in SPF mice, both of which were less pronounced in the microglia of GF mice (Fig. 2i and Extended Data Figs. 2b and 4h). Our data indicate that the microbiota contributes to increased oxidative stress in the microglia of the aged brain, which is associated with direct damage to the mitochondria.

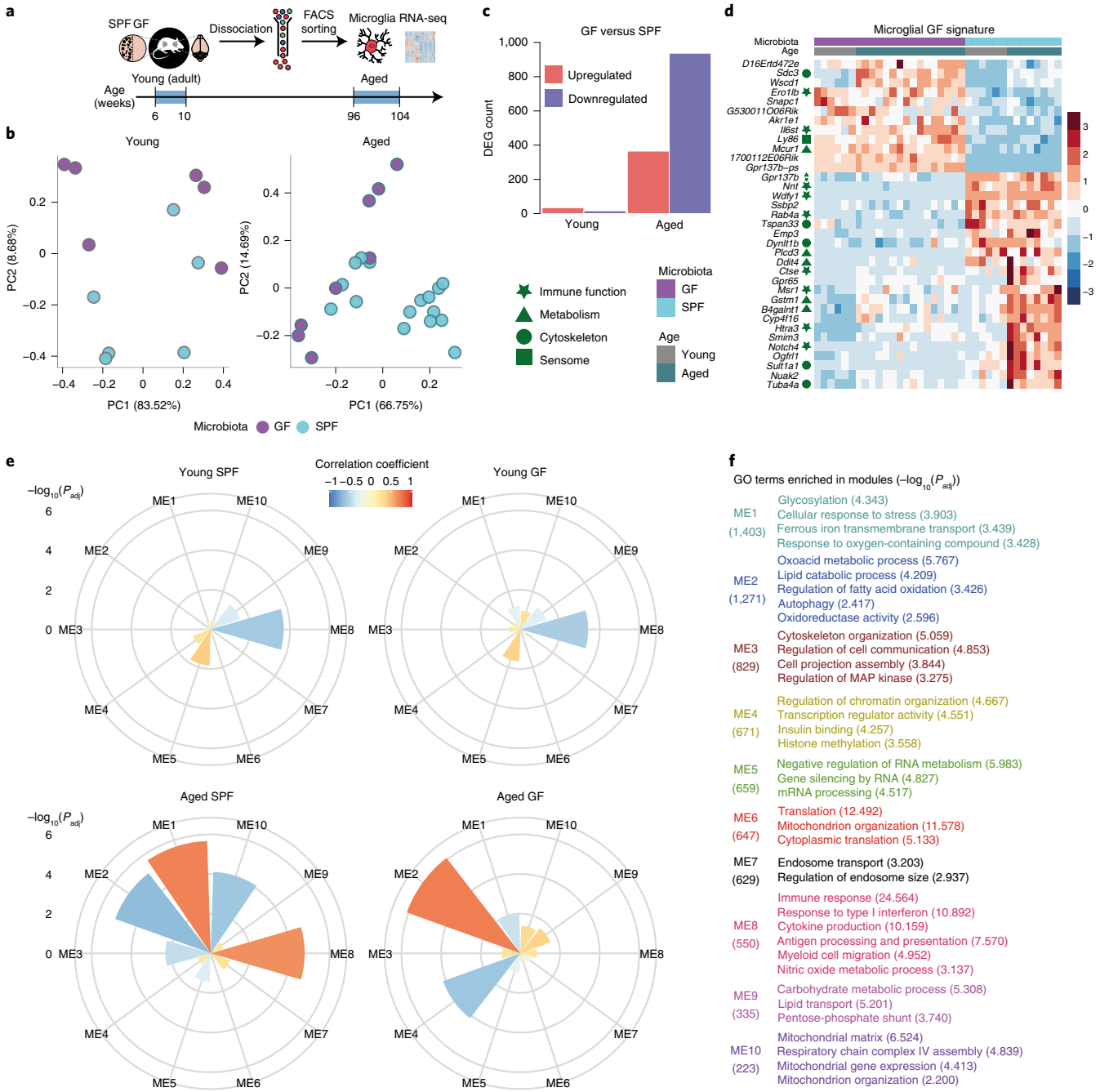

Fig. 1 | Microbiota orchestrates microglial transcriptome in young and aged mice. a, Schematic diagram of the experimental setting: RNA-seq of FACS-isolated microglia from the whole brain of young-adult (6–10-week-old) and aged (96–104-week-old) SPF and GF mice. **b**, PCA on transcriptome (normalized gene counts) of microglia isolated from young-adult and aged SPF ($n = 6, 16$) and GF ($n = 6, 8$) mice. **c**, Number of upregulated and downregulated DEGs in GF versus SPF mice across the age groups. **d**, Microglial GF signature: heatmap of a subset of DEGs in GF versus SPF mice independent of age. The list of genes with symbols (left) indicates their functional annotation (bottom left). Each column is a biological replicate and each row is a gene. DEGs (Wald $P_{adj} < 0.05$ and absolute fold change ≥ 1.5). *z*-scores were calculated from normalized gene counts (upregulation in red, downregulation in blue). **e**, Module-trait correlation across ages. Each subplot represents a different group with the depiction of all MEs extracted by WGCNA (color: correlation coefficient; radius: scaled $-\log_{10}(P_{adj})$). **f**, Significant Gene Ontology (GO) terms enriched in modules with the respective $-\log_{10}(P_{adj})$. The number of genes per module (ME1–ME10) are shown. **e**,**f**, Two-sided *P* values were obtained by Wald test and corrected for multiple testing using the Benjamini–Hochberg method.

Microbiota-dependent accumulation of CML with age. Considering the age-related changes in the microbiota, we sought to identify the metabolites involved in microglial aging by examining metabolites whose presence in serum and brain tissue is modulated with age. Short-chain fatty acids (SCFAs) are an important group of metabolites that modulate microglial function in adult mice[5,25]. We determined the concentrations of SCFAs in the serum samples of young-adult and aged SPF mice using targeted liquid chromatography–mass spectrometry (LC–MS) metabolite analysis (Fig. 3a). Elevated concentrations of acetate and propionate were

found in the sera of aged mice compared to young-adult mice. Butyrate/isobutyrate and valerate/isovalerate were not changed (Fig. 3a). To apply a more unbiased screening, we reexamined a nontargeted metabolomics dataset from our recent study[14] and focused on blood serum and brain samples from young-adult and aged mice housed under SPF conditions (Fig. 3b,c and Supplementary Table 5). Pathway enrichment analysis revealed several tissue-specific pathway alterations. For example, pyrimidine, inositol, carnitine and several pathways related to amino acid metabolism (for example, lysine, polyamine and tyrosine) were more affected in the serum of aged mice (Extended Data Fig. 5a). Vitamin A, tocopherol, purine metabolism, ceramide-related pathways and the pentose phosphate pathway were specifically altered in the brains of aged mice (Extended Data Fig. 5b). Pathways of fatty acid metabolism and advanced glycation end products (AGEs) were commonly altered in both serum and brain samples of aged mice (Extended Data Fig. 5a,b). Since we sought to identify metabolites that were potentially regulated by the gut and reached the brain via the bloodstream, we focused on metabolites that were significantly upregulated in both the serum and brain tissue of aged mice. These metabolites included palmitoleate (16:1n7), trimethylamine *N*-oxide (TMAO), 1-oleoyl-2-docosahexaenoyl-glycerophosphorylcholine (18:1/22:6), CML and stachydrine (Fig. 3d). Some of the age-related concentration changes seen in mice were confirmed in human blood samples (Supplementary Table 6). Nontargeted metabolomics on serum/plasma from a human aging cohort (TwinsUK data bank) recapitulated the age-related concentration changes of CML (Fig. 3e) and TMAO (Fig. 3f) as seen in mice. Targeted metabolomics from the brain tissue of young and aged SPF and GF mice indicated that a functional gut microbiota (SPF) was necessary for the increase in CML and TMAO in aged mouse brain tissue. Aged GF mice displayed only minor changes compared to young GF mice (Fig. 3g).

CML enhances age-related microglial dysfunction. The next step was to investigate the functional effects of these metabolites on microglia in vivo. Based on the most striking changes found in samples from mice and humans but absent in aged GF mice, we selected the following candidate metabolites for further evaluation: CML, TMAO, acetate and propionate. CML and TMAO were previously shown to increase in aging brains[26,27], while SCFAs, like acetate, have a key role in microbiota–gut–brain cross talk[5,28–30]. To identify the metabolite(s) responsible for the increased ROS production in aged microglia, we administered each metabolite separately to young-adult mice. To avoid potential artifacts related to different gut-to-circulation absorption profiles, we injected young-adult mice intraperitoneally once per day for two weeks with CML, TMAO, sodium acetate or sodium propionate (Fig. 4a). TMAO, sodium acetate and sodium propionate had no effect on intracellular ROS production or on the metabolic function of microglia. However, CML treatment could partially recapitulate the changes found in the microglia of aged mice.

CML increased oxidative stress, decreased metabolic activity and reduced cellular ATP stores (Fig. 4b–d). Moreover, CML caused mitochondrial dysfunction by directly inflicting damage to mitochondrial structures in the microglia (Extended Data Fig. 5c). The impact of CML treatment was not only restricted to microglia but seemed to be detrimental for macrophages in general. Indeed, bone marrow-derived macrophages (BMDMs) showed a dose-dependent increase in oxidative stress and decreased metabolic activity in vitro (Extended Data Fig. 5d,e). Circulating CML can be derived from an endogenous Maillard reaction, food or the conversion of AGEs by the gut microbiota[31]. Although brain CML levels increased in aged SPF mice but not in aged GF mice (Fig. 4e), CML was still detectable in the brain tissue of young-adult and aged GF mice to a similar level to that of young-adult SPF mice. This suggests that the gut microbiota is required for increased CML levels in the aged brain but not for the baseline levels found in young-adult mice. Therefore, these results suggest that the deregulation of mitochondrial function in microglia seen after intraperitoneal injection of CML resulted from increased brain CML concentrations, recapitulating the settings in aged brains (Fig. 4f). RNA-seq analysis of microglia indicated that intraperitoneal injection of CML upregulated the expression of the ROS-related genes *S100a9* and *S100A8* and other microbiota- and aging-related genes, such as *A430033K04Rik*, *Chic1*, *Ltf*, *Ngp*, *Pglyrp1*, *Scai* and *Zkscan2* (Fig. 4g,h, Extended Data Fig. 5f and Supplementary Table 7).

We then investigated whether microglia are directly targeted by CML. Immunofluorescence staining of CML in the cortical microglia of mice that were housed under SPF and GF conditions showed an increase in the percentage of CML$^+$ microglia with age. While approximately 30% of microglia in aged SPF mice was CML$^+$, the microglia of aged GF mice showed less age-dependent accumulation of CML (Fig. 4i,j). Furthermore, we verified whether the age-dependent increase in CML$^+$ microglia seen in the mouse cortex was also present in the human cortex. We obtained human brain tissues (total $n=43$; males$=23$, females$=20$) from individuals between the ages of 1 and 88 years. We observed a positive correlation ($r=0.5793$, $R^2=0.3356$, $P<0.001$) between age and the percentage of CML$^+$ microglia in the human cortex (Fig. 4k,l). These findings suggest that the age-related accumulation of CML induces microglial metabolic dysfunction in a direct fashion, including increased ROS, and may gradually disrupt brain homeostasis and brain function.

Aged microbiota fuels CML levels by disrupting the gut–blood barrier. Since we observed differences in CML levels and microglial function especially at an old age, which were dependent on the presence or absence of the microbiota, we opted to characterize the age-dependent gut microbiota alterations by 16S ribosomal RNA-seq. The distinctiveness of the microbiota profile of young-adult and aged mice was confirmed by Beta diversity analysis using the Bray–Curtis dissimilarity metric and the Shannon and

Fig. 2 | Microbiota contributes to age-related oxidative stress and mitochondrial dysfunction in microglia. a, ROS-associated MEs (top to bottom: ME1, ME2, ME8) (color: correlation coefficient; diameter: scaled $-\log_{10}(P_{adj})$). **b**, Heatmap of ROS-related genes in MEs (1, 2, 8) in the microglia of young-adult and aged SPF and GF mice. Each column is a biological replicate. **c**, Quantification of cellular ROS relative to young-adult SPF mice. Data are presented as mean values + s.e.m. from 3 independent experiments including SPF ($n=18$, 14) and GF ($n=13$, 10). **d**, Quantification of iNOS$^+$ Iba-1$^+$ area in microglia relative to young-adult SPF mice. Data are presented as mean values + s.e.m. from two experiments and include SPF ($n=14$, 9) and GF ($n=10$, 9). **e**, Immunofluorescence of Iba-1 (red), iNOS (green) and DAPI (blue) in the cortex of aging SPF and GF mice. Scale bar, 40 µm. **f**, Metabolism-associated ME10 (color: correlation coefficient; diameter: scaled $\log_{10}(P_{adj})$). **g**, Percentage of healthy versus abnormal mitochondria in the cortical microglia of aged SPF and GF mice. Each dot represents an average of 30–35 cells from 1 mouse. Data are presented as mean values + s.e.m. from two independent experiments including aged SPF and GF mice ($n=8$ each). **h**, Electron micrographs of microglia from aged SPF and GF mice. Blue arrowheads, healthy; red arrowheads: abnormal. Scale bar, 2 µm. Magnified micrographs of mitochondrial morphologies. Scale bar, 500 nm. **i**, Mitochondrial activity in microglia relative to young-adult SPF mice. Data are presented as mean values + s.e.m. from 3 experiments including SPF ($n=17$, 14) and GF ($n=9$, 13). Each dot represents one mouse. **c**,**d**,**i**, Two-way ANOVA followed by Tukey's post-hoc test. **g**, Two-way ANOVA followed by Sidak's multiple comparisons test (*$P<0.05$, **$P<0.01$, ***$P<0.001$; NS, not significant). Exact *P* values are reported in the source data.

Simpson Alpha diversity metrics (Extended Data Fig. 6a,b). The gut microbiota in both age groups was dominated by two phyla (Extended Data Fig. 6c), namely *Firmicutes* and *Bacteroidetes*. The relative abundance ratio of *Firmicutes* to *Bacteroidetes* is altered with advanced age in humans and can be linked to overall changes in bacterial profiles at different age stages[32]. We observed a significant

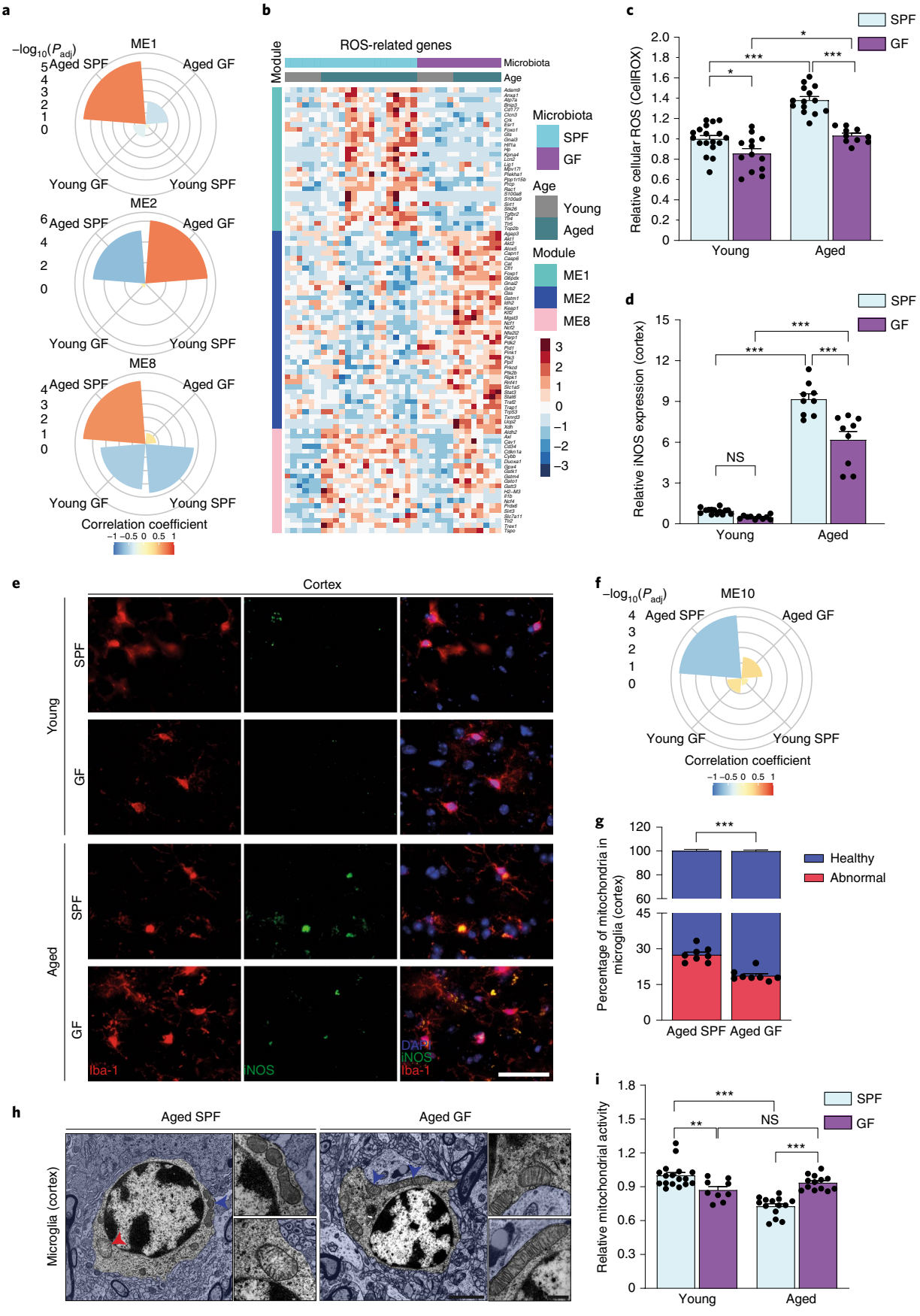

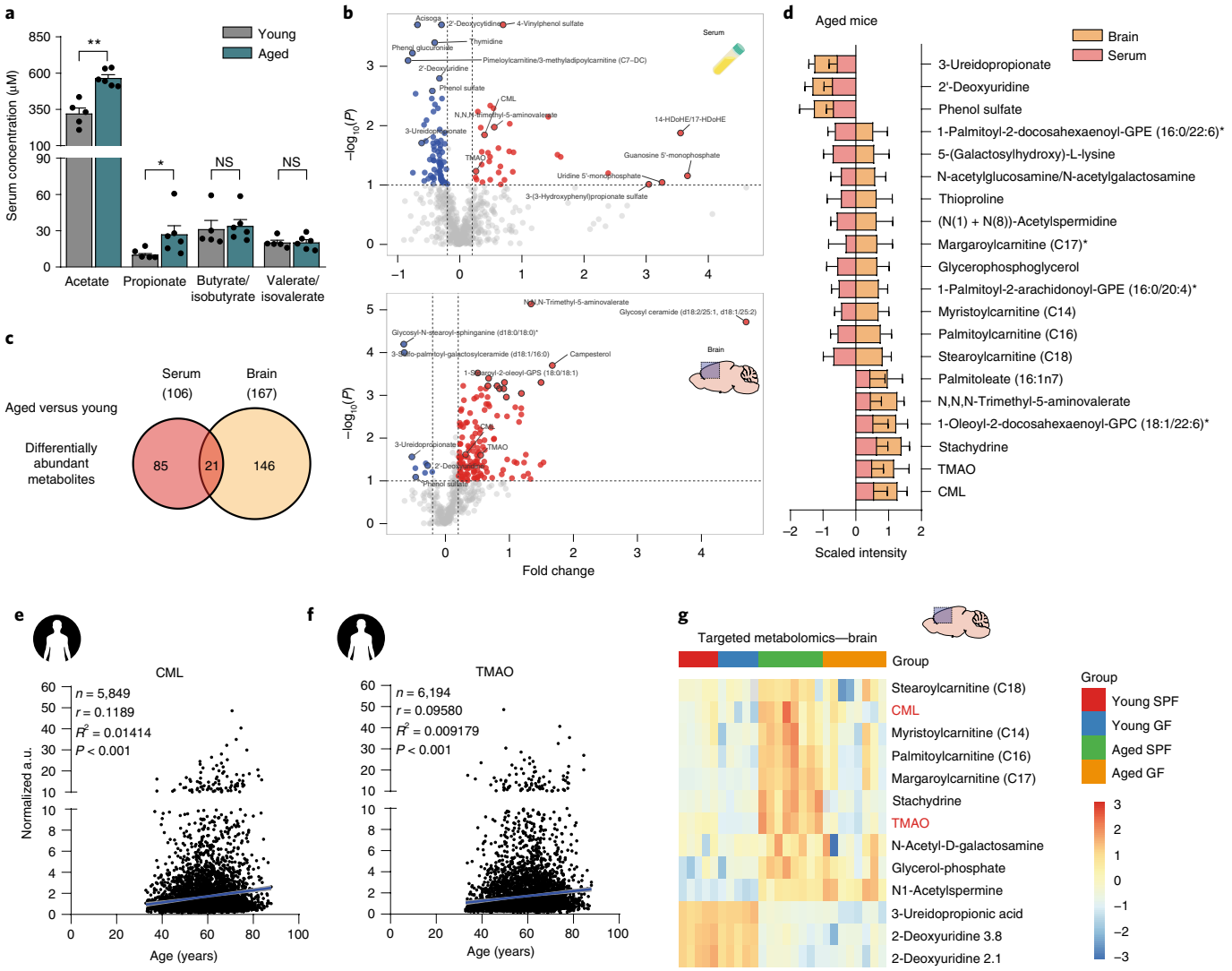

Fig. 3 | Microbiota- and age-associated regulation of serum and brain metabolites. a, SCFA concentration in serum samples. Each dot represents one mouse. Data presented as mean values + s.e.m. from 1 experiment including young-adult and aged SPF mice ($n = 5, 6$). **b**, Volcano plots of differentially abundant metabolites from nontargeted metabolomics analysis of serum (top: $n = 5, 6$) and brain tissue (bottom: $n = 5, 5$) samples of young-adult and aged SPF mice. *x* axis: Fold change. *y* axis: $-\log_{10}(P)$. Red, upregulated; blue, downregulated. **c**, Differentially abundant metabolites from serum (106) and brain (164) samples; intercept (19). **d**, Metabolites that were differentially abundant in aging for both serum and brain specimens. Biochemical name: the asterisk indicates a compound that has not been confirmed based on a standard. **e**,**f**, Dot plots of CML (**e**) and TMAO (**f**) quantified by nontargeted metabolomics on serum in a human aging cohort (when detectable) from the TwinsUK data bank. Data are presented from Long et al.[55] ($n = 6{,}194$). Center line: Best-fit value of the slope and intercept and error bars (95% confidence intervals (CIs)). a.u., arbitrary unit. **g**, Heatmap depicting a subset of metabolites by targeted metabolomics on the brain of young-adult and aged SPF and GF mice (young-adult mice, $n = 5$; aged mice, $n = 8$ each). Each column represents data from one animal and each row represents a metabolite. **a**, Two-sided Mann–Whitney *U*-test. **e**,**f**, Two-sided Pearson correlation analysis ($^*P < 0.05$, $^{**}P < 0.01$). Exact *P* values are reported in the source data.

age-dependent reduction in the *Firmicutes* to *Bacteroidetes* ratio, where the phylum *Firmicutes*, family Lachnospiraceae was significantly diminished in aged mice (Extended Data Fig. 6d,e). When we had a closer look at bacterial genera, we found an increased abundance of *Turibacter*, *Alloprevotella*, *Parasutterella*, *Bifidobacterium*, *Macellibacteroides*, *Alistipes* sensu stricto 1, *Peptostreptococcaceae incertae sedis* and *Parabacteroides* in aged mice. This was in contrast to the abundance of *Pantoea*, *Anoxybacillus*, Lachnospiraceae incertae sedis, *Cutrobacterium* and *Acetatifactor*, which declined in aged mice (Extended Data Fig. 6f and Supplementary Table 8). Thus, we can infer that profiling microbiota in young-adult and aged mice indicated alterations at several taxonomic levels. Since CML levels were more elevated in the brains of aged SPF mice than aged GF mice, we expected a microbiota-dependent production of CML. Targeted metabolomics (LC–MS) measurements of CML in fecal pellets revealed the exact reverse: fecal pellets of aged GF mice had higher CML levels than those from aged SPF mice, suggesting an indirect role of the microbiota in the age-related accumulation of CML in the brain (Fig. 5a).

Aged mice showed increased intestinal permeability compared to young-adult mice[33], a phenomenon that is dependent on the presence of the microbiota[34]. Increased permeability allows metabolites to pass from inside the gastrointestinal tract through the intestinal epithelium more freely and enter the bloodstream, which could explain the discrepancy between CML levels in the brain and feces. To test this hypothesis, we first measured intestinal permeability by

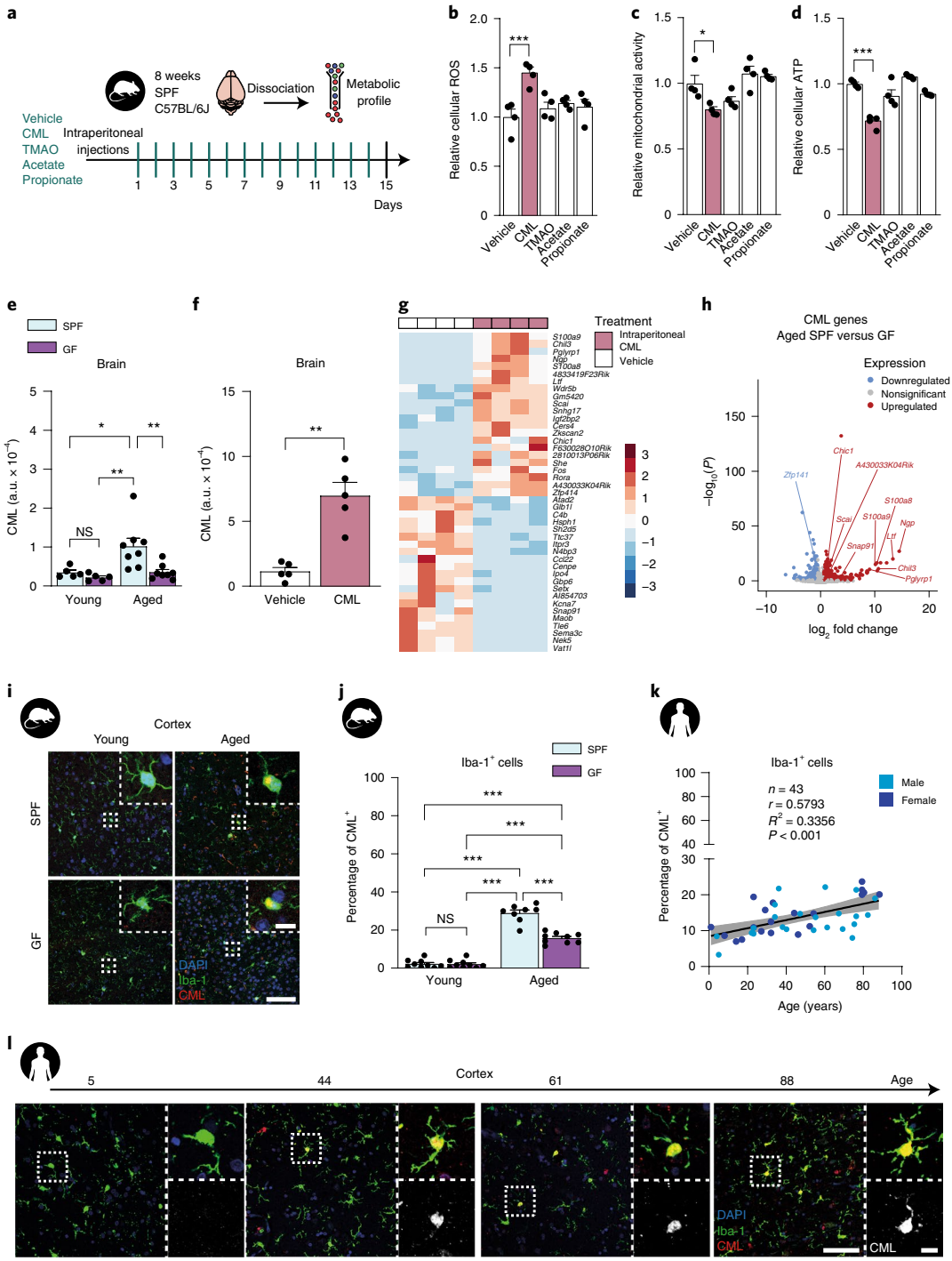

Fig. 4 | CML contributes to microbiota-mediated microglial aging. a, Schematic of metabolite treatment. Young-adult SPF mice treated intraperitoneally with CML, TMAO, sodium acetate or sodium propionate daily for two weeks. **b**, Quantification of ROS. **c**, Mitochondrial activity. **d**, ATP. **b**,**c**,**d**, Each dot represents one mouse and was depicted relative to vehicle-treated mice ($n=4$). Data are presented as mean values + s.e.m. **e**, Quantification of CML by targeted metabolomics in the brain; groups are as in Fig. 3g. Data are presented as mean values + s.e.m. from SPF and GF mice (young-adult, $n=5$; aged, $n=8$ each). **f**, Brain of vehicle-treated or CML-injected young-adult SPF mice ($n=5$). **g**, Heatmap depicting DEGs in the microglia of CML versus vehicle-injected mice. Each column is a biological replicate and each row is a gene. DEGs (Wald test $P_{adj} < 0.05$ and absolute fold change ≥ 1.5). Upregulation in red and downregulation in blue. **h**, Volcano plot of DEGs in SPF versus GF microglia from aged mice (dots) with CML-specific genes (labeled). **i**, Immunofluorescence of CML (red), Iba-1 (green) and DAPI (blue) in the mouse cortex of young-adult and aged SPF and GF mice. Scale bars, 50 µm (overview) and 10 µm (inset). **j**, Percentage of CML$^+$ Iba-1$^+$ cells in the mouse cortex of young-adult and aged SPF ($n=9, 8$) and GF ($n=9, 9$) mice. Data are presented as mean values + s.e.m. **k**, Linear regression between the percentage of CML$^+$ Iba-1$^+$ cells and age in the human cortex. Each dot represents 1 individual ($n=43$; Pearson correlation analysis: $r=0.5793$, $R^2=0.3356$, $P<0.001$). Males, $n=23$, light blue. Females, $n=20$, dark blue. Age, 1–88 years. Center line: Best-fit value of the slope and intercept. Error bars: 95% CIs. **l**, Immunofluorescence of CML (red), Iba-1 (green) and DAPI (blue) in the human cortex. Scale bars, 50 µm (overview) and 10 µm (inset). **f**, Two-sided Mann–Whitney *U*-test. **k**, Two-sided Pearson correlation analysis. **b**–**d**, One-way ANOVA followed by Dunnett's post-hoc test. **e**,**j**, Two-way ANOVA followed by Tukey's post-hoc test (*$P<0.05$, **$P<0.01$, ***$P<0.001$). Exact *P* values are reported in the source data.

quantifying the translocation of FITC-dextran (4 kDa) to the circulation after oral gavage. We observed high gut permeability in aged SPF mice but the barrier function in aged GF mice appeared to be equivalent to that of young-adult SPF and GF mice (Fig. 5b). Colonization of young-adult GF mice with aged microbiota induced a microbiota-dependent increase in intestinal permeability compared to the permeability found after young-adult GF mice had received young gut microbiota (Fig. 5c). This aligned with the observation that the translocation of CML into the circulation after oral gavage was highest in aged SPF mice (Fig. 5d and Extended Data Fig. 7a). We next sought to assess whether different routes of CML application would influence the accumulation of CML in microglia. Young-adult mice that had received CML intraperitoneally, rather than by oral gavage administration, showed more CML^+ microglia in the cortex (Extended Data Fig. 7b,c). In aged mice, the route of CML administration had no notable effect on the percentage of CML^+ microglia (Extended Data Fig. 7b,c). However, CML application by both intraperitoneal and oral gavage routes significantly exacerbated the age-related increase in cellular ROS and diminished metabolic function in microglia from aged mice. In young-adult mice, such an effect was only detectable after intraperitoneal administration of CML (Extended Data Fig. 7d,e). Finally, to verify the key role of the gut barrier to the age-related accumulation of CML in microglia, we treated aged SPF mice (18 months old) every 3 d for 10 weeks orally with ellagic acid (EA), which prevents accumulation of CML[35], or intestinal alkaline phosphatase (IAP), an endogenous enhancer of the gut barrier function, by reducing the age-related microbiota dysbiosis and inducing autophagy in the gut epithelium[36,37] (Fig. 5e). While EA had no effect on gut permeability, IAP-treated aged mice showed lower gut leakiness (Fig. 5f). However, both EA and IAP reduced CML accumulation in the brain (Fig. 5g). The microglia of EA- and IAP-treated aged mice showed a significant reduction in cellular ROS and increased ATP levels compared to vehicle-treated aged mice (Fig. 5h,i). These findings underline the impact of age-induced microbiota alterations, which disrupt the integrity of the gut barrier and facilitate the accumulation of CML in the brains of aged mice and humans (Fig. 5j).

Discussion

In this study, we examined the contribution of the host microbiota to the age-related physiology of microglia by comparing young-adult and aged mice housed under SPF and GF conditions. By combining nontargeted metabolomics analyses on serum and brain tissue with IHC, we found an age-dependent accumulation of CML in the microglia of mice and humans. Increased levels of CML with age were caused by the microbiota-dependent increase in intestinal permeability. Thus, heightened oxidative stress and mitochondrial dysfunction were detectable.

Our findings in SPF mice confirmed that aged microglia display morphological changes[3], while the microglia of aged GF mice retained their hyper-ramified morphology seen in young-adult GF mice[5]. This morphological phenotype could be possibly linked to the cytoskeletal genes, annotated in the microglial GF signature, and genes in ME2 that regulate cell morphogenesis. Moreover, we found substantial differences in the microglial transcriptional profile between aged and young-adult mice, summarized in the gene modules ME1 and ME8, which confirms previous research[38,39]. The enhanced expression of genes in the age-related MEs was absent in aged GF animals, indicating that the microbiota determines microglial activation and is crucial for regulating processes like the immune response, cytokine production and Toll-like receptor signaling in microglia of the aged brain. This observation clearly shows that microglial aging depends on the presence of a complex gut microbiota.

One aspect of the age-related changes in microglia is the induction of oxidative stress by the overproduction of ROS[40]. We observed a microbiota-dependent differential regulation of ROS-related genes in aged mice. Detailed analyses confirmed the increase in ROS levels in microglia even in the absence of a microbiota; however, the microglia of GF mice had consistently lower levels of ROS relative to SPF controls. Oxidative stress may not only contribute to cognitive decline and early onset of chronic neurodegenerative diseases[19,41] but can also disrupt the physiology of microglia themselves. ROS can damage the mitochondria by inducing mitochondrial DNA mutations, altering mitochondrial membrane permeability, disrupting Ca^{2+} homeostasis and damaging the respiratory chain leading to mitochondrial and cellular dysfunction[42]. For this reason, mitochondria are thought to be the primary target of oxidative damage, which occurs already in middle-aged mice[43,44]. We did not find differences in mitochondrial density or mass between the microglia of aged SPF and GF mice. However, we observed a disruption of mitochondrial integrity in microglia from aged SPF mice, a process that was far less pronounced in aged GF mice, as indicated by fewer damaged mitochondria and increased cellular ATP levels compared to aged SPF mice. In addition, only in microglia from aged SPF mice, the increased cellular ROS was coupled to the transcriptional activation of *Hif1a*, a known regulator of cellular energy metabolism that can drive shifts toward glycolysis[45]. Our findings clearly point toward the contribution of the microbiota to the regulation of microglial energy homeostasis in aged mice.

Therefore, we sought a more comprehensive mechanistic understanding of the relationship between the gut microbiota and microglial aging. Nontargeted metabolomics revealed metabolites related to AGE products, amino acid and nucleotide metabolism, and long-chain fatty acid metabolism to be differentially changed in both the sera and brains of aged mice. The concentration of only a few metabolites from the serum and brain samples was significantly altered in the same directions. In many cases, metabolites were regulated in opposite directions in blood serum and brain tissue. Most metabolites were regulated in opposite directions in blood serum and brain tissue, with brain tissue having higher concentrations than serum. Most lipid-insoluble compounds from the bloodstream are substantially slowed by the presence of the blood–brain barrier in the brain. However, the various transport systems and receptors expressed on endothelial cells accelerate the blood–brain barrier penetration of a number of different metabolites and are sufficient to build up and maintain a concentration gradient between the blood serum and the brain. Out of the four metabolites tested, TMAO, CML, acetate and propionate, only CML replicated the age-associated oxidative stress and metabolic dysfunction in microglia. SCFAs, such as acetate and propionate, represent established mechanisms by which the intestinal microbiota regulates the maturation and function of microglia[5]. It is therefore surprising that acetate and propionate had no effect on intracellular ROS production or on the mitochondrial function of microglia. If at all, then only specific SCFAs seemed to affect ROS production as seen in microglia-like HL-60 cells, where formate, but not valerate, reduced the production of ROS[46]. CML is a major AGE found in different tissues and blood serum in multiple age-related diseases and has been shown to be a ligand of receptor for advanced glycation end products (RAGE)[47–50]. However, only CML bound to a peptidic structure is capable of binding to RAGE[51]. Our quantification methods did not differentiate peptide-bound from free CML.

The intestines host a diverse microbial community that modifies and shapes the composition of the metabolites and chemical signals within the gut. It was previously described that aged humans[11] and mice[12,52] have a different gut microbiota composition compared to younger adults. We observed a drop in the *Firmicutes* to *Bacteroidetes* ratio in aged mice and a similar scenario was reported in humans[53]. In particular, bacteria of the Lachnospiraceae family were reduced in aged mice and have been found to maintain gut barrier integrity, which correlates with intestinal permeability[54].

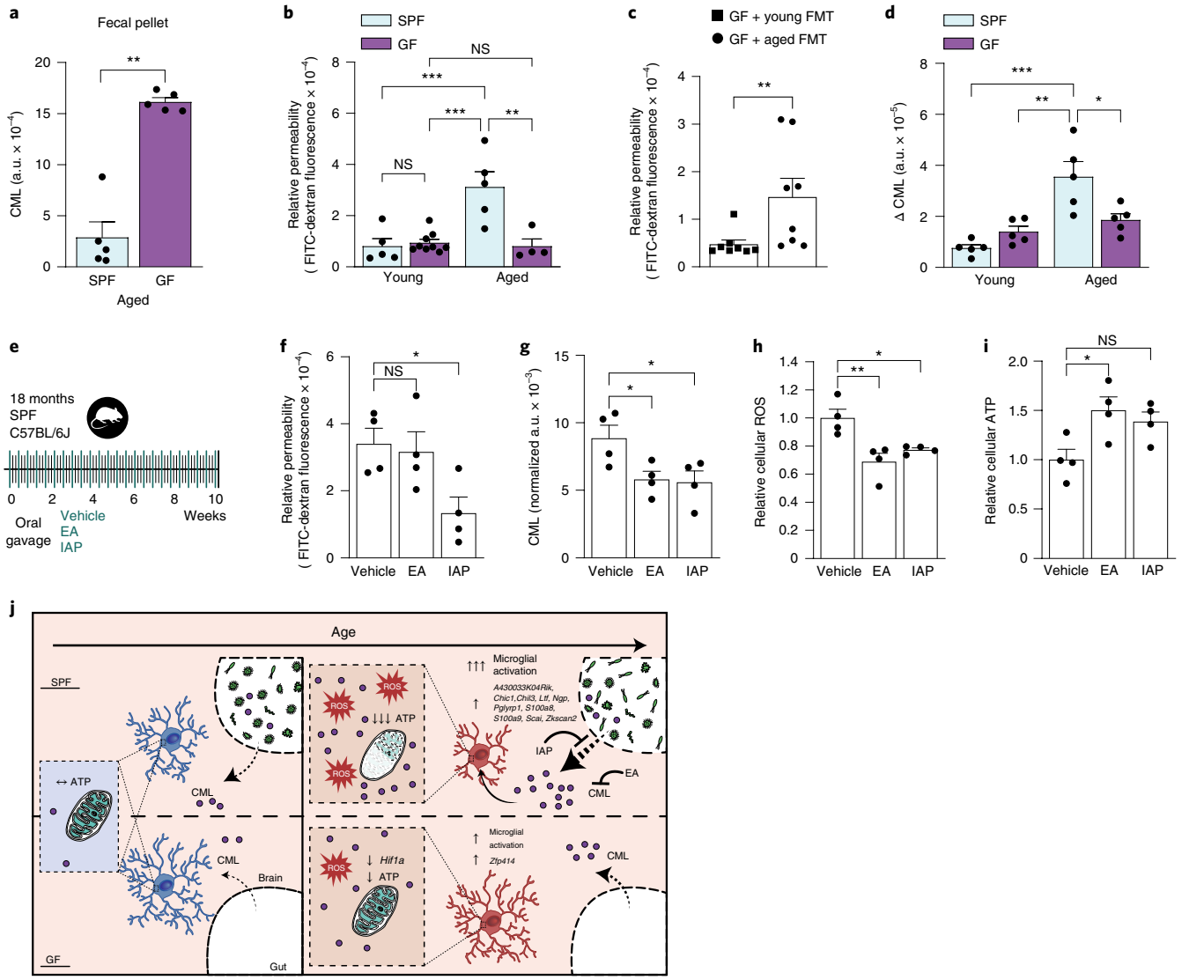

Fig. 5 | Disruption of gut–blood barrier in aging instigates CML surge. a, Quantification of CML by targeted metabolomics (LC–MS) in fecal pellets freshly obtained from aged SPF and GF mice ($n=5$). **b**,**c**, Intestinal permeability measured by the percentage of fluorescent FITC-dextran (4 kDa) translocation to the circulation after oral gavage in young-adult and aged mice housed under SPF ($n=5$, 5) or GF ($n=9$, 4) conditions (**b**) and young-adult GF mice that received young or aged fecal microbiota transplantation (FMT) ($n=8$) (**c**). **d**, Difference in CML translocated into the circulation 4 h post-oral gavage in young-adult and aged mice housed under SPF or GF ($n=5$) conditions. **e**, Schematic diagram: (e-i) 18-month-old SPF mice were treated orally every third day for 10 weeks with vehicle (20% hydroxypropyl-β-cyclodextrin in 1× PBS), EA or IAP ($n=4$). **f**, Intestinal permeability measured by the percentage of fluorescent FITC-dextran (4 kDa) translocation to the circulation after oral gavage. **g**, Quantification of CML by targeted metabolomics (LC–MS) in the brain. **h**, Quantification of relative mean fluorescence intensity of the CellROX probe signal. **i**, Quantification of relative cellular ATP. **a**,**c**, Two-sided Mann–Whitney *U*-test. **f**–**i**, One-way ANOVA followed by Dunnett's post-hoc test. **b**,**d**, Two-way ANOVA followed by Tukey's post-hoc test (*$P<0.05$, **$P<0.01$, ***$P<0.001$). Exact *P* values are reported in the source data. Data are presented as mean values + s.e.m. **j**, Schematic of gut microbiota-mediated CML accumulation in the aged brain. CML induces aging features in microglia, specifically oxidative stress and mitochondrial damage. Rejuvenating the gut–blood barrier integrity limits CML accumulation and its detrimental effects on microglia.

Considering that age-related changes in gut microbiota are associated with increased gut permeability at older ages, it is conceivable that metabolites and other factors of the gut microbiota may alter microglial function, particularly in the aged brain.

Higher CML blood levels during aging are not necessarily the result of augmented production of CML by the gut microbiota or an increased intake through food. Instead, our findings strongly support the idea that CML might more easily pass the intestinal mucosal barrier in aged animals as a result of the increased gut permeability present in aged mice[33,34]. Indeed, when CML was administered intraperitoneally, thus bypassing uptake by the intestinal wall, it elicited microglial activation and metabolic dysfunction in both young-adult and aged mice. When CML was administered by oral gavage, the microglia in young-adult mice were unaffected but the microglia in aged mice were adversely impacted. Moreover, aged mice raised under GF conditions showed less accumulation of CML in microglia compared to SPF housed mice, despite higher amounts of CML present in their feces. As shown in our gut–blood translocation experiments, the intact gut epithelium in aged GF mice prevented excessive uptake of CML from the intestine into the bloodstream and subsequent microglial dysfunction.

In conclusion, we identified and verified the critical involvement of CML in oxidative stress and mitochondrial dysfunction in the microglia of aged mice. Oral administration of CML to young-adult mice had virtually no negative impact on microglial homeostasis. The facilitated egress of CML from the gut into the circulation is required for CML to manifest its harmful impact. The gut microbiota, which changes in composition with age, introduces elevated intestinal permeability at older ages and plays a key role in this process. All of these mechanisms play an important part in microglial aging and are expected to have a role in the overall aging of the murine but also human CNS.

Online content

Any methods, additional references, Nature Research reporting summaries, source data, extended data, supplementary information, acknowledgements, peer review information; details of author contributions and competing interests; and statements of data and code availability are available at https://doi.org/10.1038/s41593-022-01027-3.

Received: 2 February 2021; Accepted: 28 January 2022;
Published online: 3 March 2022

References

1. Prinz, M., Masuda, T., Wheeler, M. A. & Quintana, F. J. Microglia and central nervous system-associated macrophages—from origin to disease modulation. *Annu. Rev. Immunol.* **39**, 251–277 (2021).
2. Salter, M. W. & Beggs, S. Sublime microglia: expanding roles for the guardians of the CNS. *Cell* **158**, 15–24 (2014).
3. Streit, W. J., Sammons, N. W., Kuhns, A. J. & Sparks, D. L. Dystrophic microglia in the aging human brain. *Glia* **45**, 208–212 (2004).
4. Johnson, K. V. & Foster, K. R. Why does the microbiome affect behaviour? *Nat. Rev. Microbiol.* **16**, 647–655 (2018).
5. Erny, D. et al. Host microbiota constantly control maturation and function of microglia in the CNS. *Nat. Neurosci.* **18**, 965–977 (2015).
6. Matcovitch-Natan, O. et al. Microglia development follows a stepwise program to regulate brain homeostasis. *Science* **353**, aad8670 (2016).
7. Thion, M. S. et al. Microbiome influences prenatal and adult microglia in a sex-specific manner. *Cell* **172**, 500–516.e516 (2018).
8. Abdel-Haq, R., Schlachetzki, J. C. M., Glass, C. K. & Mazmanian, S. K. Microbiome–microglia connections via the gut–brain axis. *J. Exp. Med.* **216**, 41–59 (2019).
9. Mossad, O. & Blank, T. Getting on in old age: how the gut microbiota interferes with brain innate immunity. *Front. Cell. Neurosci.* **15**, 698126 (2021).
10. Lakshminarayanan, B., Stanton, C., O'Toole, P. W. & Ross, R. P. Compositional dynamics of the human intestinal microbiota with aging: implications for health. *J. Nutr. Health Aging* **18**, 773–786 (2014).
11. O'Toole, P. W. & Jeffery, I. B. Gut microbiota and aging. *Science* **350**, 1214–1215 (2015).
12. Langille, M. G. et al. Microbial shifts in the aging mouse gut. *Microbiome* **2**, 50 (2014).
13. Boehme, M. et al. Microbiota from young mice counteracts selective age-associated behavioral deficits. *Nat. Aging* **1**, 666–676 (2021).
14. Mossad, O. et al. Microbiota-dependent increase in δ-valerobetaine alters neuronal function and is responsible for age-related cognitive decline. *Nat. Aging* **1**, 1127–1136 (2021).
15. Uchimura, Y. et al. Antibodies set boundaries limiting microbial metabolite penetration and the resultant mammalian host response. *Immunity* **49**, 545–559.e5 (2018).
16. Tremblay, M.-È., Zettel, M. L., Ison, J. R., Allen, P. D. & Majewska, A. K. Effects of aging and sensory loss on glial cells in mouse visual and auditory cortices. *Glia* **60**, 541–558 (2012).
17. Langfelder, P. & Horvath, S. WGCNA: an R package for weighted correlation network analysis. *BMC Bioinformatics* **9**, 559 (2008).
18. Baker, D. J. et al. Clearance of p16Ink4a-positive senescent cells delays ageing-associated disorders. *Nature* **479**, 232–236 (2011).
19. Streit, W. J. Microglial senescence: does the brain's immune system have an expiration date? *Trends Neurosci.* **29**, 506–510 (2006).
20. Sun, J., Druhan, L. J. & Zweier, J. L. Reactive oxygen and nitrogen species regulate inducible nitric oxide synthase function shifting the balance of nitric oxide and superoxide production. *Arch. Biochem. Biophys.* **494**, 130–137 (2010).
21. Zhao, K., Huang, Z., Lu, H., Zhou, J. & Wei, T. Induction of inducible nitric oxide synthase increases the production of reactive oxygen species in RAW264.7 macrophages. *Biosci. Rep.* **30**, 233–241 (2010).
22. Stefanatos, R. & Sanz, A. The role of mitochondrial ROS in the aging brain. *FEBS Lett.* **592**, 743–758 (2018).
23. Gomes, A. P. et al. Declining NAD^+ induces a pseudohypoxic state disrupting nuclear-mitochondrial communication during aging. *Cell* **155**, 1624–1638 (2013).
24. López-Otín, C., Blasco, M. A., Partridge, L., Serrano, M. & Kroemer, G. The hallmarks of aging. *Cell* **153**, 1194–1217 (2013).
25. Shi, H. et al. A fiber-deprived diet causes cognitive impairment and hippocampal microglia-mediated synaptic loss through the gut microbiota and metabolites. *Microbiome* **9**, 223 (2021).
26. Thangthaeng, N., Sumien, N. & Forster, M. J. Dissociation of functional status from accrual of CML and RAGE in the aged mouse brain. *Exp. Gerontol.* **43**, 1077–1085 (2008).
27. Ke, Y. et al. Gut flora-dependent metabolite trimethylamine-N-oxide accelerates endothelial cell senescence and vascular aging through oxidative stress. *Free Radic. Biol. Med.* **116**, 88–100 (2018).
28. Colombo, A. V. et al. Microbiota-derived short chain fatty acids modulate microglia and promote Aβ plaque deposition. *eLife* **10**, e59826 (2021).
29. Erny, D. et al. Microbiota-derived acetate enables the metabolic fitness of the brain innate immune system during health and disease. *Cell Metab.* **33**, 2260–2276.e7 (2021).
30. Mezö, C. et al. Different effects of constitutive and induced microbiota modulation on microglia in a mouse model of Alzheimer's disease. *Acta Neuropathol. Commun.* **8**, 119 (2020).
31. Tessier, F. J. et al. Quantitative assessment of organ distribution of dietary protein-bound ^{13}C-labeled N^{ε}-carboxymethyllysine after a chronic oral exposure in mice. *Mol. Nutr. Food Res.* **60**, 2446–2456 (2016).
32. Mariat, D. et al. The *Firmicutes*/*Bacteroidetes* ratio of the human microbiota changes with age. *BMC Microbiol.* **9**, 123 (2009).
33. Hayes, C. L. et al. Commensal microbiota induces colonic barrier structure and functions that contribute to homeostasis. *Sci. Rep.* **8**, 14184 (2018).
34. Thevaranjan, N. et al. Age-associated microbial dysbiosis promotes intestinal permeability, systemic inflammation, and macrophage dysfunction. *Cell Host Microbe* **21**, 455–466.e4 (2017).
35. Raghu, G., Jakhotia, S., Yadagiri Reddy, P., Kumar, P. A. & Bhanuprakash Reddy, G. Ellagic acid inhibits non-enzymatic glycation and prevents proteinuria in diabetic rats. *Food Funct.* **7**, 1574–1583 (2016).
36. Kühn, F. et al. Intestinal alkaline phosphatase targets the gut barrier to prevent aging. *JCI Insight* **5**, e134049 (2020).
37. Singh, S. B., Carroll-Portillo, A., Coffman, C., Ritz, N. L. & Lin, H. C. Intestinal alkaline phosphatase exerts anti-inflammatory effects against lipopolysaccharide by inducing autophagy. *Sci. Rep.* **10**, 3107 (2020).
38. Grabert, K. et al. Microglial brain region-dependent diversity and selective regional sensitivities to aging. *Nat. Neurosci.* **19**, 504–516 (2016).
39. Hammond, T. R. et al. Single-cell RNA sequencing of microglia throughout the mouse lifespan and in the injured brain reveals complex cell-state changes. *Immunity* **50**, 253–271.e6 (2019).
40. Koellhoffer, E. C., McCullough, L. D. & Ritzel, R. M. Old maids: aging and its impact on microglia function. *Int. J. Mol. Sci.* **18**, 769 (2017).
41. Kettenmann, H., Kirchhoff, F. & Verkhratsky, A. Microglia: new roles for the synaptic stripper. *Neuron* **77**, 10–18 (2013).
42. Guo, C., Sun, L., Chen, X. & Zhang, D. Oxidative stress, mitochondrial damage and neurodegenerative diseases. *Neural Regen. Res.* **8**, 2003–2014 (2013).
43. Enciu, A.-M., Gherghiceanu, M. & Popescu, B. O. Triggers and effectors of oxidative stress at blood–brain barrier level: relevance for brain ageing and neurodegeneration. *Oxid. Med. Cell. Longev.* **2013**, 297512 (2013).
44. Luceri, C. et al. Aging related changes in circulating reactive oxygen species (ROS) and protein carbonyls are indicative of liver oxidative injury. *Toxicol. Rep.* **5**, 141–145 (2018).
45. Cramer, T. et al. HIF-1α is essential for myeloid cell-mediated inflammation. *Cell* **112**, 645–657 (2003).
46. Wenzel, T. J., Gates, E. J., Ranger, A. L. & Klegeris, A. Short-chain fatty acids (SCFAs) alone or in combination regulate select immune functions of microglia-like cells. *Mol. Cell. Neurosci.* **105**, 103493 (2020).
47. Basta, G. et al. Advanced glycation end products activate endothelium through signal-transduction receptor RAGE: a mechanism for amplification of inflammatory responses. *Circulation* **105**, 816–822 (2002).
48. Dyer, D. G. et al. Accumulation of Maillard reaction products in skin collagen in diabetes and aging. *J. Clin. Invest.* **91**, 2463–2469 (1993).
49. Gironès, X. et al. N^{ε}-carboxymethyllysine in brain aging, diabetes mellitus, and Alzheimer's disease. *Free Radic. Biol. Med.* **36**, 1241–1247 (2004).
50. Wong, A. et al. Advanced glycation endproducts co-localize with inducible nitric oxide synthase in Alzheimer's disease. *Brain Res.* **920**, 32–40 (2001).
51. Xue, J. et al. Advanced glycation end product recognition by the receptor for AGEs. *Structure* **19**, 722–732 (2011).
52. Spychala, M. S. et al. Age-related changes in the gut microbiota influence systemic inflammation and stroke outcome. *Ann. Neurol.* **84**, 23–36 (2018).

53. Vaiserman, A. et al. Differences in the gut *Firmicutes* to *Bacteroidetes* ratio across age groups in healthy Ukrainian population. *BMC Microbiol.* **20**, 221 (2020).
54. Hu, S. et al. Anti-inflammation effects of fucosylated chondroitin sulphate from *Acaudina molpadioides* by altering gut microbiota in obese mice. *Food Funct.* **10**, 1736–1746 (2019).
55. Long, T. et al. Whole-genome sequencing identifies common-to-rare variants associated with human blood metabolites. *Nat. Genet.* **49**, 568–578 (2017).

Methods

Human tissue. Formalin-fixed paraffin-embedded (FFPE) cortical tissue from healthy brains was examined by a fully trained neuropathologist (control tissue or Braak stages I and II) from 43 individuals (20 females and 23 males aged 1–88 years; 8 temporal, 25 frontal lobe) at the Institute of Neuropathology, University Hospital Freiburg, Germany.

Mice. SPF and GF housed C57BL/6 mice were analyzed at 6–10 (young-adult) and 96–104 (aged) weeks of age. Mice of the aged group in the nontargeted metabolomics analysis were 17–18 months old. Except for nontargeted metabolomics and microbiota profiling, where male mice were used, all groups included mice from both sexes. Mice were housed under a 12-h light/12-h dark cycle and temperatures of 18–23 °C with 40–60% humidity, with food and water given ad libitum. To avoid cage effects, mice from at least three different cages per experimental group were analyzed. For the metabolite treatment, young-adult mice (8 weeks old) were injected intraperitoneally or by oral gavage with CML (0.735 mg kg^{-1}; Iris Biotech), TMAO (3.95 mg kg^{-1}; Sigma-Aldrich), sodium acetate (59 mg kg^{-1}; Sigma-Aldrich) and sodium propionate (4.61 mg kg^{-1}; Sigma-Aldrich) daily for 14 d. For modulation of CML in aged animals, 18-month-old SPF housed C57BL/6 mice were treated orally every third day for 10 weeks with vehicle (20% hydroxypropyl-β-cyclodextrin in 1× PBS), 10 mg kg^{-1} EA or 3,000 U kg^{-1} IAP. To assess in vivo intestinal permeability, tracer fluorescein isothiocyanate (FITC)-labeled dextran (4 kDa; Sigma-Aldrich) was used as previously[34]. Briefly, mice were deprived of food 4 h before and both food and water 4 h after oral gavage using 200 µl of 80 mg ml^{-1} FITC-dextran. Blood was collected retro-orbitally after 4 h and fluorescence intensity was measured on fluorescence plates using an excitation wavelength of 493 nm and an emission wavelength of 518 nm. To assess in vivo intestinal permeability to CML, mice were treated with 200 µl CML (0.36 mM). Blood was collected retro-orbitally immediately before and 4 h after treatment. CML translocated into the circulation was measured by LC–MS. All animal experiments were approved by the local administration in Germany (Regierungspräsidium Freiburg) and were performed in accordance with the respective national, federal and institutional regulations and the guidelines of the Federation of European Laboratory Animal Science Associations.

Preparation of mouse tissue samples. Mice were lethally anesthetized with ketamine (100 mg kg^{-1} body weight) and xylazine (10 mg kg^{-1} body weight) followed by perfusion with 1× PBS through the left heart chamber. For histology, brains were kept overnight in 4% paraformaldehyde (PFA). For flow cytometry and magnetic-activated cell sorting (MACS) beads cell sorting, brains were dissected, homogenized and filtered through a 70-µm mesh. After centrifugation (220 *g* for 5 min at 4 °C), pellets were resuspended in 37% Percoll followed by centrifugation for 30 min, 800 *g* at 4 °C. Myelin was removed from the top layer and the cell pellet was washed once with 1× PBS followed by antibody staining.

IHC. Brains were fixed in 4% PFA overnight and embedded in paraffin. Three micrometer-thick parasagittal sections were stained with anti-Iba-1 antibody (1:500 dilution, catalog no. 019-19741; WAKO) to assess microglial cell density. For IHC, epitopes were unmasked by heat-induced antigen retrieval at pH 6. The primary antibody was incubated overnight (4 °C) followed by incubation with biotin-labeled goat anti-rabbit secondary antibodies (1:1,000 dilution; SouthernBiotech) for 45 min at room temperature. Streptavidin-horseradish peroxidase (SouthernBiotech) was then added for 45 min at room temperature. 3,3′-Diaminobenzidine brown chromogen (Dako) was used to resolve the antibody's signal. Nuclei were counterstained with hematoxylin. Images were acquired with the BZ-9000 Biorevo microscope (Keyence) and analyzed with the ImageJ v. 1.53f (National Institutes of Health) software.

Immunofluorescence. Brains were fixed in 4% PFA, dehydrated in 30% sucrose and embedded in Tissue-Tek OCT compound (Sakura Finetek). Fourteen micrometer-thick cryosections were obtained using a cryostat (SM2000R; Leica Biosystems). FFPE tissue from mouse and human brains was sectioned by a microtome to obtain 5-µm sections. Epitopes were unmasked by heat-induced antigen retrieval at pH 6. Sections were blocked with PBS containing 5% BSA and permeabilized with 0.5% Triton X-100 in blocking solution. The following primary antibodies were incubated overnight at 4 °C: rabbit anti-Iba-1 (1:500 dilution; WAKO); guinea pig anti-Iba-1 (1:1,000 dilution; Synaptic Systems); anti-iNOS (1:500 dilution; Thermo Fisher Scientific) or anti-CML (1:500; Abcam). Secondary antibodies (Alexa Fluor 488-, 568- or 647-conjugated, 1:500 dilution) were incubated for 2 h at room temperature. For three dimensional (3D)-reconstruction of microglia, free-floating 30-µm cryosections from brain tissue were labeled for 48 h with anti-Iba-1 (1:500 dilution) at 4 °C, followed by Alexa Fluor 647-conjugated secondary antibody at a dilution of 1:500 overnight at 4 °C. Slides were treated with TrueBlack Lipofuscin Autofluorescence Quencher to eliminate autofluorescence in tissue from aged mice and human individuals. Nuclei were counterstained with 4′,6-diamidino-2-phenylindole (DAPI). Coverslips were mounted with ProLong Diamond Antifade Mountant (Thermo Fisher Scientific). Images were acquired using a BZ-9000 Biorevo microscope using a 20×/0.75 numerical aperture (NA) objective, an Olympus Fluoview 1000 confocal laser scanning microscope or with a TCS SP8 X (Leica Microsystems) using a 20×/0.75 NA objective (HC PL APO 20×/0.75 NA IMM CORR CS2). For 3D-reconstruction of microglia, images were analyzed using Imaris v.8.02 (Bitplane) with at least five cells per mouse. All other images were processed and analyzed with Photoshop CC 2015 (Adobe) or ImageJ v. 1.53f (National Institutes of Health).

Electron microscopy. Brain specimens from the cortex were first fixed overnight in 3% glutaraldehyde at 4 °C, washed with Sörensen buffer and then transferred to 1% osmium tetroxide for 2 h at room temperature. Next, samples were dehydrated by a graded series of ethanol (30–100%) followed by 100% propylene oxide, resin/propylene oxide (1:2 (v/v)) and resin/propylene oxide (2:1 (v/v)). Samples were embedded in resin via polymerization for 24 h at 75 °C. Then, 700-nm semithin sections were cut and stained with 2% toluidine blue to define the region of interest for further preparation of 70-nm ultrathin sections using an ultramicrotome (Leica Reichert Ultracut S) after contrasting the sections with uranyl acetate and lead citrate (Leica Reichert Ultrastainer). To assess the mitochondrial phenotype in microglia, images were acquired with a ×7,900 or ×46,000 magnification using a CM100 electron microscope (Philips). Images of 30–35 cells per mouse were processed and analyzed with the iTEM software 2012 (Olympus).

BMDM cell culture. Cells were cultured at 37 °C and 5% CO_2 in a humidified incubator. Murine BMDMs were differentiated from tibial and femoral bone marrow aspirates. Recombinant murine macrophage colony-stimulating factor (Immunotools) was used at 20 ng ml^{-1}. After 7 d of differentiation, BMDMs were seeded in 24-well plates with 5×10^5 cells per well in triplicates. The medium was switched to serum-free medium 6 h before the experiment. Cells were incubated with increasing concentrations of CML (untreated, 0.1 µM, 1 µM, 10 µM, 100 µM, 1 mM) for 48 h, then collected for measurements.

Flow cytometry. Cell sorting for RT–qPCR and RNA-seq was performed on a MoFlo Astrios (Beckman Coulter; Extended Data Fig. 2a). Before surface staining, dead cells were excluded by using the Fixable Viability Dye eFluor 780 (1:1,000 dilution; Thermo Fisher Scientific) followed by incubation with Fc receptor blocking antibody CD16/CD32 (1:200 dilution, clone 2.4G2; BD Bioscience). The following antibodies were used for surface staining: anti-CD45 (1:200 dilution, clone 30-F11; Thermo Fisher Scientific); anti-CD11b (1:200 dilution, clone M1/70; Thermo Fisher Scientific). The following lineage antibodies were used (all at 1:300 dilution): anti-CD3 (clone 17A2; BioLegend); anti-CD19 (clone 6D5; BioLegend); anti-CD45R (clone RA3-6B2; BD Biosciences); Ly6C (clone AL-21; BD Biosciences); Ly6G (clone 1A8; BD Biosciences). To assess microglial cellular ROS, we used the CellROX DeepRed Reagent (5 µM; Thermo Fisher Scientific). To assess mitochondrial activity, we used Tetramethylrhodamine, Methyl Ester, Perchlorate (50 nM; Thermo Fisher Scientific) and MitoTracker Green FM (20 nM; Thermo Fisher Scientific). Dead cells were excluded by short incubation with DAPI before flow cytometry analysis with the FACSCanto II (BD Biosciences). Data were acquired with the FACSDiva v.6 software (Becton Dickinson). Postacquisition analysis was performed with FlowJo v.10 (FlowJo LLC).

Cellular ATP measurement. To avoid the cellular stress of FACS sorting, microglial cells were isolated using the MACS cell separation system (Miltenyi Biotec; Extended Data Fig. 2b). The cell suspension was incubated with Fc receptor blocking antibody CD16/CD32 (clone 2.4G2; BD Biosciences) and with biotinylated anti-CD11b antibody (clone M1/70; Thermo Fisher Scientific). Anti-biotin microbeads (Miltenyi Biotec) were then added to the cell suspension and positive selection was carried out according to the manufacturer's instructions. From each sample, 10,000 cells per well were plated in 96-well plates in triplicates. Cellular ATP was measured using the CellTiter-Glo assay (Promega Corporation) according to the manufacturer's instructions.

RNA-seq. Total RNA was extracted from FACS-sorted CD11b$^+$CD45^{int}Lin$^-$ microglia (10,000 cells per sample) using the Arcturus PicoPure RNA Isolation Kit (Thermo Fisher Scientific) according to the manufacturer's protocol. The SMARTer v4 Ultra Low Input RNA Kit for Sequencing (Clontech) was used to generate first-stranded complementary DNA. Double-stranded cDNA was amplified by long-distance PCR (11 cycles) and purified via magnetic bead cleanup. Library preparation was carried out as described in the Illumina Nextera XT sample preparation guide (Illumina). The sequencing run was performed on a HiSeq 1000 instrument (Illumina) using the indexed, 50-cycle single-read protocol and the TruSeq SBS v3 Reagents according to the HiSeq 1000 system user guide. BCL files were converted into FASTQ files with the CASAVA1.8.2 software. Library preparation and RNA-seq were performed at the Genomics Core Facility 'Center of Excellence for Fluorescent Bioanalytics', University of Regensburg, Germany.

The quality of sequencing reads stored in the FASTQ files was assessed with FastQC v.0.67 and trimmed with Trim Galore! v.0.4.3. Reads were mapped on the mouse genome version mm10 (University of California Santa Cruz) using STAR aligner v.2.5.2 with RefGene annotation. The number of reads mapped to each gene (counts) was extracted from the BAM files using FeatureCount v.1.5.3. The process to extract the gene counts from FASTQ files was run on the Galaxy platform[56]. Three samples with a low mapping rate (<75%) were removed.

Differential expression analysis was performed with DESeq2 v.1.32.0. Normalized counts generated by DESeq2 were assessed for artifacts or contamination by other cell types. The list of genes used was based on single-cell RNA-seq data previously obtained by our group[57]. R v.4.1.0 was used to perform the Ward error sum of squares hierarchical clustering method and PCA. Using the DESeq2 model, differentially expressed genes (DEGs) with adjusted $P < 0.05$ (Wald test) and absolute fold change >1.5 were identified. Heatmaps were plotted using the R package pheatmap v.1.0.8 calculated from scaled (*z*-scores) normalized read counts of DEGs with a hierarchical clustering of the rows (complete method). A WGCNA was performed on normalized expression data using the R package WGCNA v.1.69 (ref. [17]). For computational efficiency, genes were filtered to keep only genes that explained more than 50% of the variance (10,848 kept genes and 7,265 removed). A module-trait correlation analysis was performed between the ME and the different traits (combination of microbiota and age) by computing the Pearson correlation between each pair of variables and Student asymptotic *P* values for the correlations using the WGCNA package. A Gene Ontology (GO) enrichment analysis of the genes in the different MEs was made using goseq v.1.44.0, with the genome-wide annotation for Mouse (org.Mm.eg.db v.3.13.0) and Wallenius approximation. The overenriched GO categories were extracted using a 0.05 false discovery rate (FDR) cutoff. The lists of ROS-related genes were extracted from GO:0000302, GO:2000377 and oxidative stress (WikiPathways).

RT–qPCR. *Hif1a* gene expression was measured using the TaqMan assay (Mm00468869_m1). Data were normalized to the value obtained from the microglia of the young-adult SPF male group at homeostasis and relative gene expression levels were determined by the $\Delta\Delta CT$ method. Gene expression was considered undetectable if the *CT* values were >35 cycles.

Microbiome profiling. As described previously[58], total DNA was isolated from fecal samples using the QIAamp DNA stool kit (QIAGEN) according to the modified manufacturer's instructions. Briefly, 100–200 mg were homogenized in 500 µl ASL buffer by the bead-beating step using TissueLyser for 3 min at 30 Hz followed by two additional lysis steps at 95 °C. Afterwards, samples were incubated with 200 µl lysis buffer for Gram$^+$ bacteria (20 mg ml^{-1} lysozyme, 20 mM Tris-HCl, pH 8.0, 2 mM EDTA, 1.2% Triton; Sigma-Aldrich). DNA was purified and pooled at a concentration of 26 pM and the pooled library was sequenced for the V5/V6 region of 16S rRNA genes in an IonTorrent PGM system according to the manufacturer's instructions (Thermo Fisher Scientific).

An average of 38,209 high-quality reads per sample were used for microbiome profiling. Reads were clustered in operational taxonomic units (OTUs) at 97% of similarity. Data were further analyzed using the QIIME v.1.9.1 pipeline after filtering out low-quality (accuracy of base calling; $q < 25$) samples; samples with ≥4,500 reads were retained for further analysis[59]. OTUs were chosen using UCLUST with a 97% sequence identity threshold followed by taxonomy assignment using the SILVA database release 119 (www.arb-silva.de). Alpha and Beta diversity were calculated using the phyloseq pipeline in R v.3.4 (refs. [60,61]). We used the nonparametric Mann–Whitney *U*-tests to compare Alpha diversity between samples and Adonis from the vegan R package v2.5-7 to assess the effects of groups for Beta diversity via phyloseq[60,61]. Taxonomic differences at the phylum and genus levels between tested groups were identified using the 'multivariate analysis by linear models' R package v0.0.4. Plots were generated with ggplot2 v.3.3.5 using a phyloseq object. Only taxa present in at least 30% of samples and OTUs comprising more than 0.0001% of total counts were considered. A $P < 0.05$ and an FDR of $q < 0.05$ (with Benjamini–Hochberg correction) were used as cutoff values for significance.

Nontargeted metabolomics. Raw data on serum and brain of young-adult and aged mice groups were mined from Mossad et al[14]. Nontargeted MS analysis was performed at Metabolon[62]. Peaks were quantified using the area under the curve. Raw area counts for each metabolite in each sample were normalized to correct for variation resulting from instrument interday tuning differences by the median value for each run day, thus setting the medians to 1.0 for each run. This preserved variation between samples but allowed metabolites of widely different raw peak areas to be compared on a similar graphical scale. Missing values were imputed with the observed minimum after normalization.

Targeted metabolomics by LC–MS. Samples were extracted with precooled (−80 °C) extraction solution (80:20 methanol LC–MS grade: Milli-Q H_2O). Targeted metabolite quantification by LC–MS was carried out using an Agilent 1290 Infinity II UHPLC system in line with an Agilent 6495 QQQ-MS operating in multiple reaction monitoring (MRM) mode. MRM settings were optimized separately for all compounds using pure standards. LC separation was on a Phenomenex Luna propylamine column (50 × 2 mm, 3-µm particles) using a solvent gradient of 100% buffer B (5 mM ammonium carbonate in 90% acetonitrile) to 90% buffer A (10 mM NH_4 in water). Flow rate was from 1,000 to 750 µl min^{-1}. The autosampler temperature was 5 degrees and the injection volume was 2 µl. Peak areas were identified based on standards for each metabolite and calculated using MassHunter v.B.08.02 (Agilent). For SCFAs, namely acetate (C2, 59.04 g mol^{-1}), propionate (C3, 73.07 g mol^{-1}), butyrate (and isobutyrate, C4, 87), valerate (and isovalerate, 101), were quantified in mouse serum. To extract the metabolites, 10 µl of each sample were added to 4 tubes, 90 µl of acetonitrile were added with serial dilution (4 levels) of standards. C2 (mg ml^{-1}) (L1:0; L2:0.002; L3:0.004; L4:0.006), C3 (mg ml^{-1}) (L1:0; L2:0.0002; L3:0.0004; L4:0.0006), C4 (mg ml^{-1}) (L1:0; L2:0.0005; L3:0.001; L4:0.0015) and C5 (%) (L1:0; L2:0.0002; L3:0.0004; L4:0.0006), C4 (mg ml^{-1}) (L1:0; L2: 0.000025%; L3: 0.00005%; L4: 0.000075%). Samples were centrifuged at 20,000 *g* for 10 min at 4 °C and 50 µl of the supernatant were transferred to a new tube. For analysis by high-performance LC–quadrupole time of flight, 2 µl of each sample were injected. Peaks of butyrate and isobutyrate, and valerate and isovalerate, could not be robustly differentiated; therefore, for each pair, concentration values correspond to both moieties. Each sample was analyzed twice and the average value was used to build the regression line; the concentration was calculated using the standard addition method[63].

Human metabolomics data. The TwinsUK adult twin registry includes about 14,000 individuals, predominantly females, with disease and lifestyle characteristic similar to the general UK population. The St. Thomas' Hospital Research Ethics Committee approved the studies and all twins provided informed written consent. We mined data for CML and TMAO from a blood metabolome study[55] that encompassed aging cohorts and was run on the Metabolon platforms. Briefly, metabolite ratios were measured in blood samples by Metabolon using an untargeted ultra-performance LC–MS/MS platform. Metabolites were scaled by run day medians and log-transformed.

Statistics. No statistical methods were used to predetermine sample sizes but our sample sizes are similar to those reported in previous publications[7,13,29]. Data distribution was assumed to be normal but this was not formally tested. Wherever applicable, animals were randomly assigned to the different experimental groups. The experimenters were blind regarding group assignments. The exact number (*n*) of replicates used in each experiment are reported in the respective figure legends. Statistical analyses, other than those of RNA-seq, nontargeted metabolomics and microbial profiling, were performed with Prism 9.0 (GraphPad Software).

Reporting Summary. Further information on research design is available in the Nature Research Reporting Summary linked to this article.

Data availability

Data on TwinsUK twin participants are available to bona fide researchers under managed access due to governance and ethical constraints. Raw data should be requested (http://twinsuk.ac.uk/resources-for-researchers/access-our-data/) and requests are going to be reviewed by the TwinsUK Resource Executive Committee regularly. Microglia RNA-seq data are available at the Gene Expression Omnibus under accession no. GSE182719. The mouse genome version mm10 (University of California Santa Cruz) can be viewed at https://www.ncbi.nlm.nih.gov/assembly/GCF_000001635.20/. For microbiome profiling, the FASTA files of two runs with their corresponding mappings are available at https://doi.org/10.6084/m9.figshare.15179775.v1 (ref. [64]). Other data that support the findings of this study are available from the corresponding author upon reasonable request. Source data are provided with this paper.

References

56. Afgan, E. et al. The Galaxy platform for accessible, reproducible and collaborative biomedical analyses: 2018 update. *Nucleic Acids Res.* **46**, W537–W544 (2018).
57. Jordão, M. J. C. et al. Single-cell profiling identifies myeloid cell subsets with distinct fates during neuroinflammation. *Science* **363**, eaat7554 (2019).
58. Yilmaz, B. et al. Microbial network disturbances in relapsing refractory Crohn's disease. *Nat. Med.* **25**, 323–336 (2019).
59. Caporaso, J. G. et al. QIIME allows analysis of high-throughput community sequencing data. *Nat. Methods* **7**, 335–336 (2010).
60. McMurdie, P. J. & Holmes, S. Phyloseq: a Bioconductor package for handling and analysis of high-throughput phylogenetic sequence data. *Pac. Symp. Biocomput.* 235–246 (2012).
61. Callahan, B. J., Sankaran, K., Fukuyama, J. A., McMurdie, P. J. & Holmes, S. P. Bioconductor workflow for microbiome data analysis: from raw reads to community analyses. *F1000Res.* **5**, 1492 (2016).
62. Evans, A. M., DeHaven, C. D., Barrett, T., Mitchell, M. & Milgram, E. Integrated, nontargeted ultrahigh performance liquid chromatography/electrospray ionization tandem mass spectrometry platform for the identification and relative quantification of the small-molecule complement of biological systems. *Anal. Chem.* **81**, 6656–6667 (2009).
63. Harris, D. C. *Quantitative Chemical Analysis* 6th edn (W H Freeman and Co., 2003).
64. Mossad, O., Yilmaz, B. & Blank, T. Dataset for gut microbiota drives age-related oxidative stress and mitochondrial damage in microglia via the metabolite N(6)-carboxymethyllysine. https://doi.org/10.6084/m9.figshare.15179775.v1 (2022).

Acknowledgements

We thank E. Barleon and K. Seidel for helping with IHC and electron microscopy. J. Bodinek-Wersing (Core Facility, University of Freiburg) was responsible for cell sorting. We thank the Metabolomics Core Facility (University of Freiburg) and in particular D. Pan for technical assistance. TwinsUK is funded by the Wellcome Trust, Medical Research Council, European Union, National Institute for Health Research-funded BioResource, Clinical Research Facility and Biomedical Research Centre based at Guy's and St. Thomas' NHS Foundation Trust in partnership with King's College London. We thank C. Moehle and T. Stempfl (University of Regensburg) for technical assistance with the RNA-seq experiments. We thank M. Havermans for providing the BMDMs. We thank A. Dumas for proofreading the manuscript. This study was funded by the Deutsche Forschungsgemeinschaft (DFG) SFB/TRR 167 to T.B., T.L., D.E., R.B. and M.P. D.E. was further supported by the Berta Ottenstein Program for Advanced Clinician Scientists. M.P. was further supported by the Sobek Foundation, Ernst-Jung Foundation, DFG (SFB 992, SFB1160, Reinhart Koselleck Grant, Gottfried Wilhelm Leibniz-Prize), Alzheimer Forschung Initiative and the Ministry of Science, Research and Arts, Baden-Württemberg ('Neuroinflammation' specialization). This study was supported by the DFG under Germany's Excellence Strategy (CIBSS, EXC-2189; project ID 390939984).

Author contributions

O.M. performed most of the experiments, helped develop the overall concept and wrote the manuscript. B.Y. and S.C.G.V. analyzed the microbiome profile within the fecal samples. M.G.D.A. bred and prepared the mice of the different age groups. B.B. and R.B. performed and designed the analyses of the RNA-seq data. E.N. and J.M.B. performed the targeted metabolomics. L.S.N., M.M., F.J.M.M., C.M. and N.D. provided help with the experiments and experimental design. T.L., A.S., A.J.M., D.E. and M.P. contributed to critical analysis of the data, developed the concepts and provided the reagents. T.B. developed the overall concept of the project, supervised the experiments and wrote the manuscript.

Competing interests

The authors declare no competing interests.

Additional information

Extended data is available for this paper at https://doi.org/10.1038/s41593-022-01027-3.

Supplementary information The online version contains supplementary material available at https://doi.org/10.1038/s41593-022-01027-3.

Correspondence and requests for materials should be addressed to Thomas Blank.

Peer review information *Nature Neuroscience* thanks John Cryan, Sarkis Mazmanian, and the other, anonymous, reviewer(s) for their contribution to the peer review of this work.

Reprints and permissions information is available at www.nature.com/reprints.

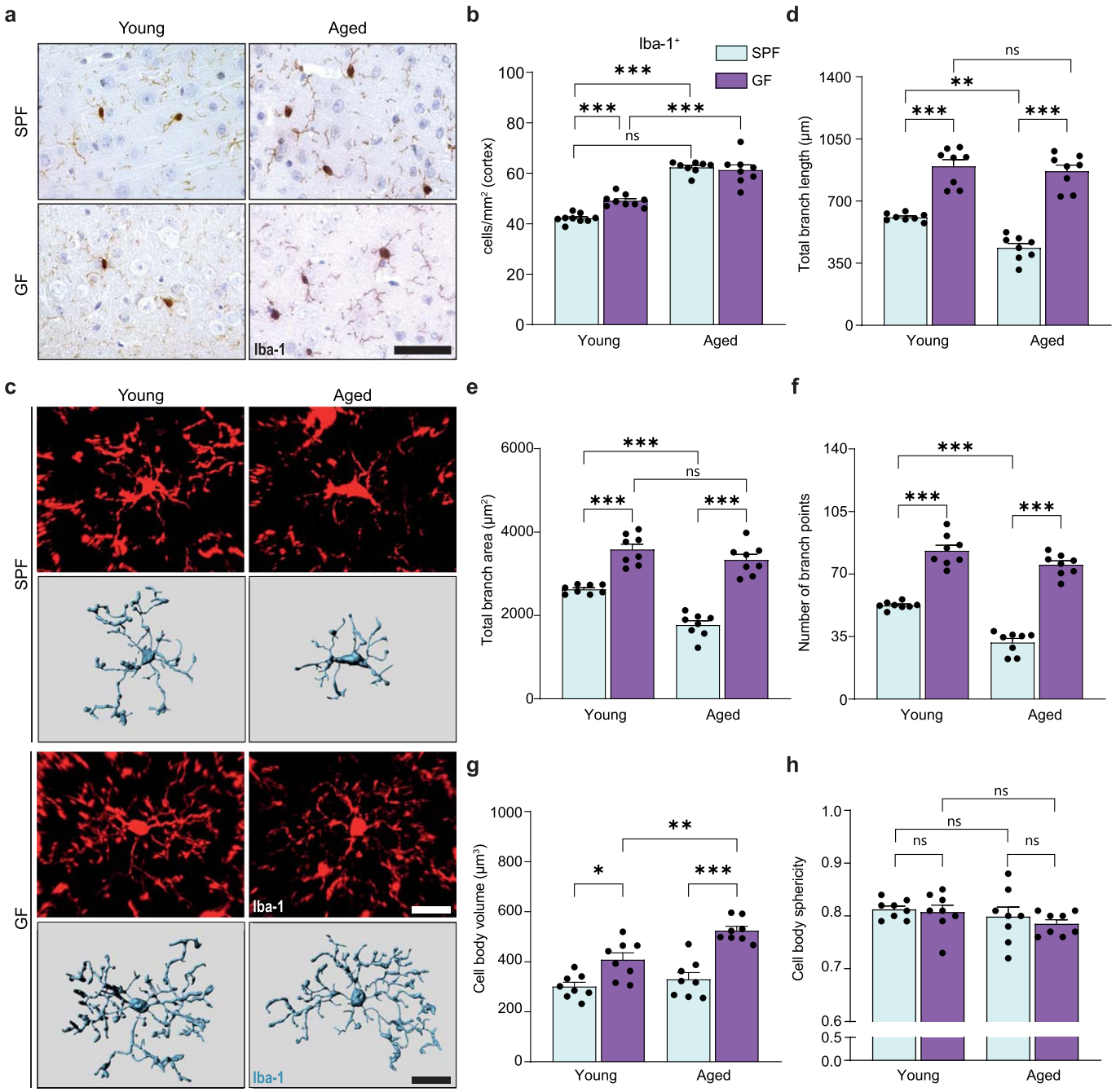

Extended Data Fig. 1 | Microglial transcriptional profile from GF and SPF mice of both sexes. (a) Heatmap of genes (normalized gene counts) specific to different types of immune cells in order to show purity of sorted cells. (b) Heatmap showing sample⁻to-sample Ward clustering. (c) Heatmap of all genes in the modules eigengenes. Each row is a biological replicate (d) Heatmap of genes in metabolism-associated module eigengene ME10. Z-scores were calculated from normalized counts. Each row is a gene, and each column is a biological replicate; microglia isolated from young-adult and aged SPF (n = 6, 16) and GF (n = 6, 8) mice.

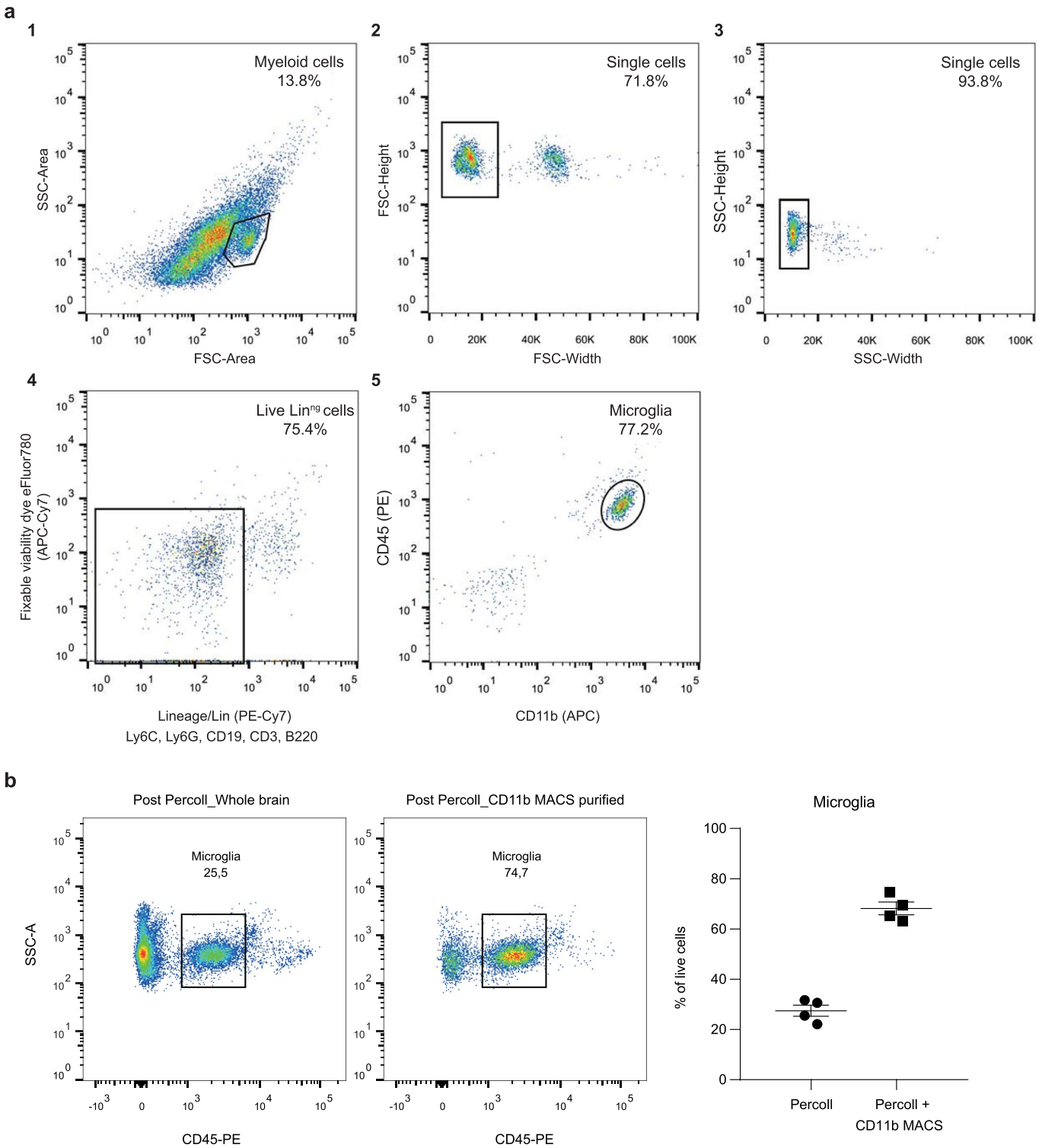

Extended Data Fig. 2 | Gating strategy for flow cytometry and purity of MACS separation. (a) Cell sorting strategy for RT-qPCR and RNA-seq. (1) Myeloid cells were gated by size and granularity then (2 and 3) only single cells were included. (4) Live and Lineage$^-$ cells were gated negative for Fixable Viability Dye eFluor® 780 and CD3, CD19, CD45R, Ly6C, and Ly6G to exclude T cells, B cells, monocytes and granulocytes, respectively. Microglia were gated on CD45^{Int} and CD11b$^+$. (b) Purity of cells used for for cellular ATP assay. Microglial cells were enriched using the CD11b MACS cell separation system (Miltenyi Biotec, USA). (b, left panel) Each dot represents one mouse. Data are presented as mean values +/- SEM.

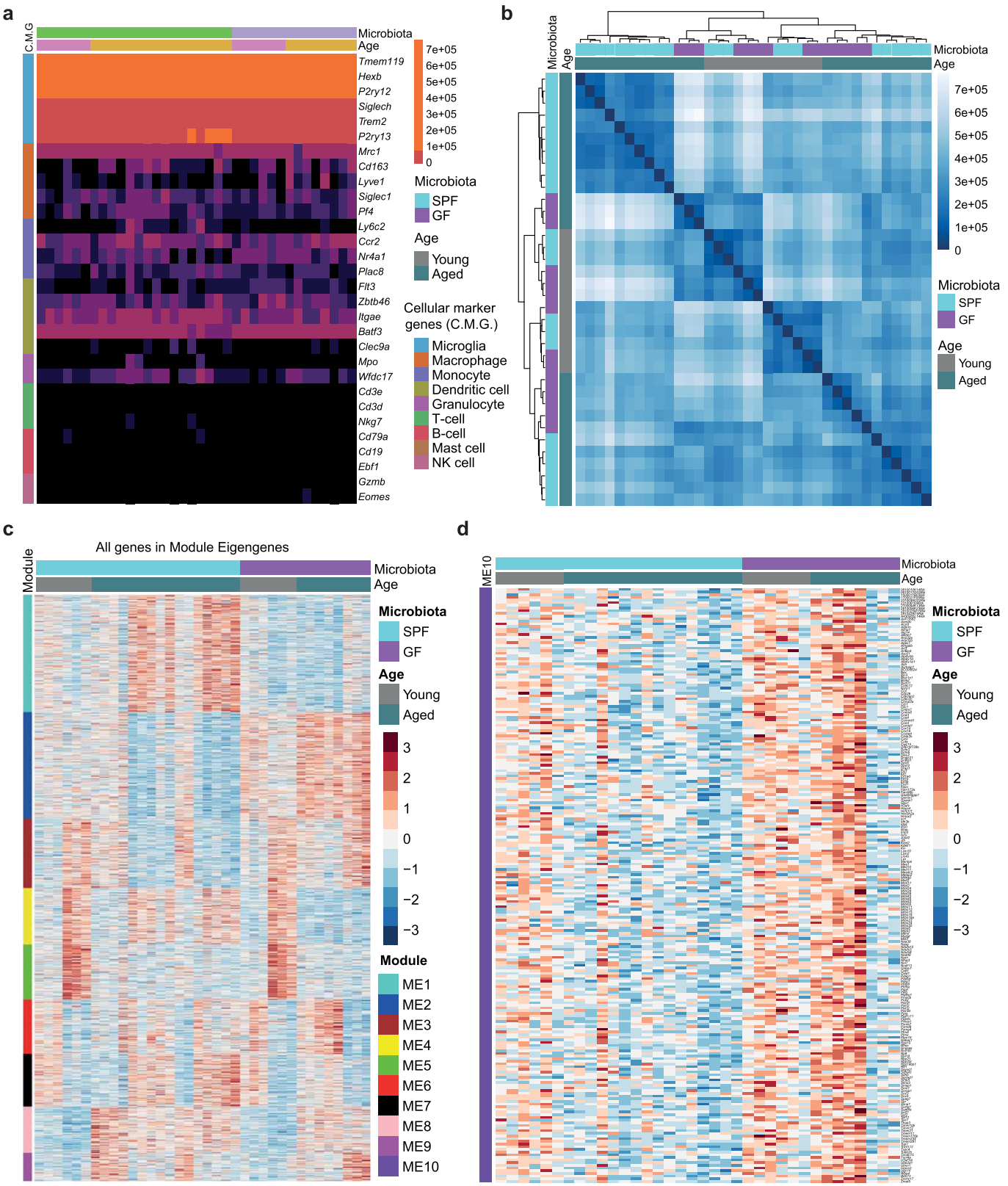

Extended Data Fig. 3 | Microbiota drives age-related differences in microglial morphology but not in cell density. (a) Immunohistological detection of Iba-1$^+$ microglia in the cortex of young-adult and aged SPF and GF mice. Scale bar, 20 µm. (b) Diagram summarizing microglia densities in the cortex. SPF (n = 9, 8) and GF (n = 9, 8). (c) Representative three-dimensional reconstruction of cortical microglia of all groups. Scale bar, 10 µm. (d-h) Imaris-based semi-automatic quantification of cell morphology. (d) Total branch length (µm), (e) total branch area (µm^2), (f) number of branch points, (g) cell body volume (µm^3) and (h) cell body sphericity. Each symbol represents an average of at least four cells measured per mouse. Data represent two independent experiments including young-adult and aged mice. SPF (n = 8, 8) and GF (n = 8, 8). Statistical analysis (b-h) two-way ANOVA followed by Tukey's post-hoc test (*$p < 0.05$, **$p < 0.01$, ***$p < 0.001$, ns = not significant). Data are presented as mean values + SEM. Exact p-values are reported in the source data.

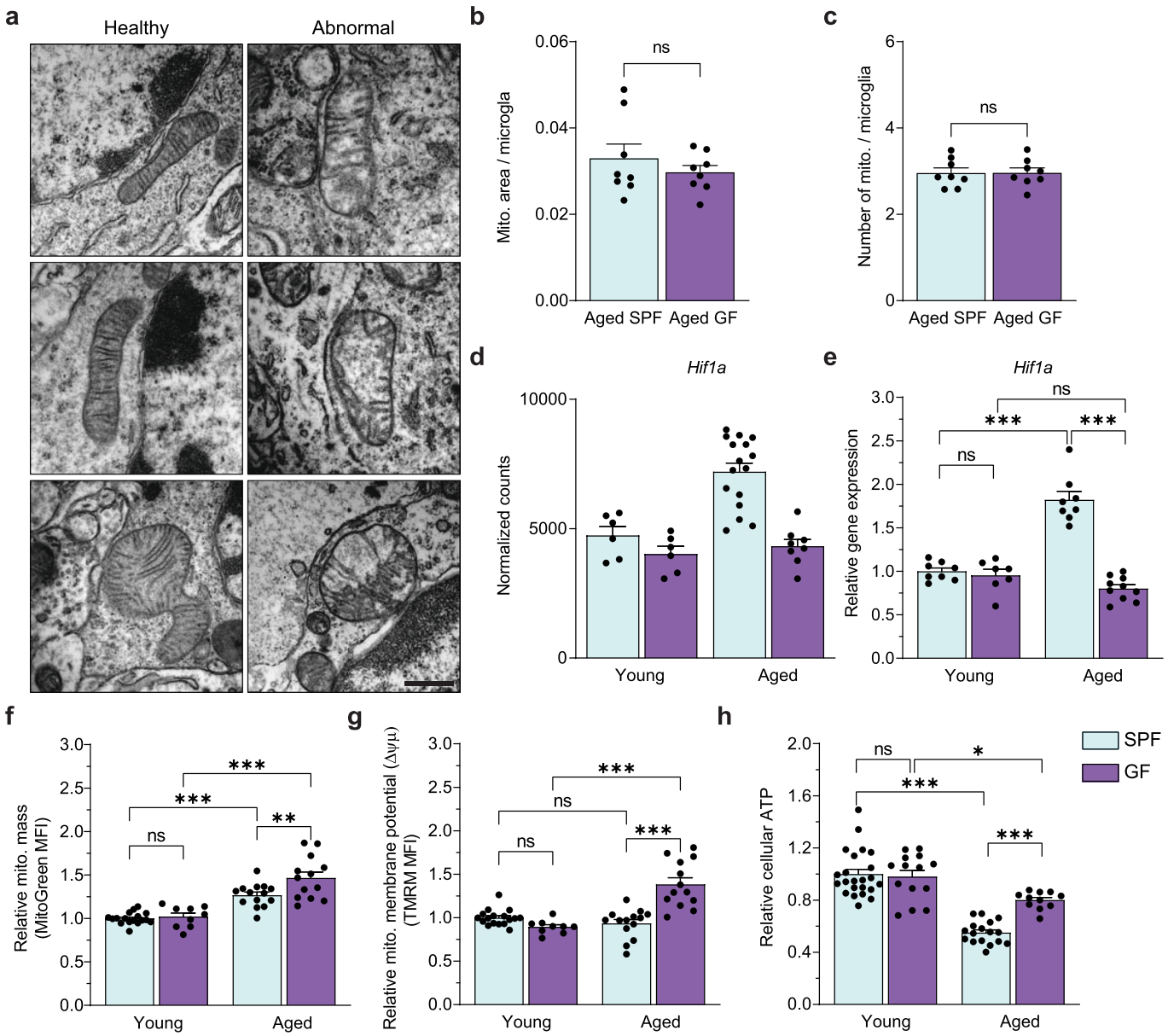

Extended Data Fig. 4 | Age-related mitochondrial physiology in microglia of male and female SPF and GF mice. (a) Representative electron micrographs of abnormal vs healthy mitochondria in cortical microglia. Scale bar, 600 nm. (b) Quantification of mitochondrial area per microglia. (c) Number of mitochondria per microglia. (b and c) Data were generated from aged SPF and GF mice (n = 8). (d) *Hif1a* mRNA expression in microglia based on RNA-seq analysis (normalized gene counts). (e) *Hif1a* mRNA expression by RT-qPCR in microglia of young-adult and aged SPF (n = 8, 8) and GF (n = 7, 10) mice. (f) Mitochondrial mass (MitoTracker Green MFI). (g) Mitochondrial membrane potential (Δψm) (TMRM dye MFI). (h) Quantification of cellular ATP relative to young-adult SPF males. Data were generated from young-adult and aged mice. (f and g) SPF (n = 17, 14) and GF (n = 9, 13). (h) SPF (n = 23, 17) and GF (n = 14, 11). (b-h) Data are presented as mean values + SEM. Statistical analysis (b and c) Mann–Whitney U test (two-sided), and (e-h) two-way ANOVA followed by Tukey's post-hoc test (*$p < 0.05$, **$p < 0.01$, ***$p < 0.001$, ns = not significant). Exact p-values are reported in the source data.

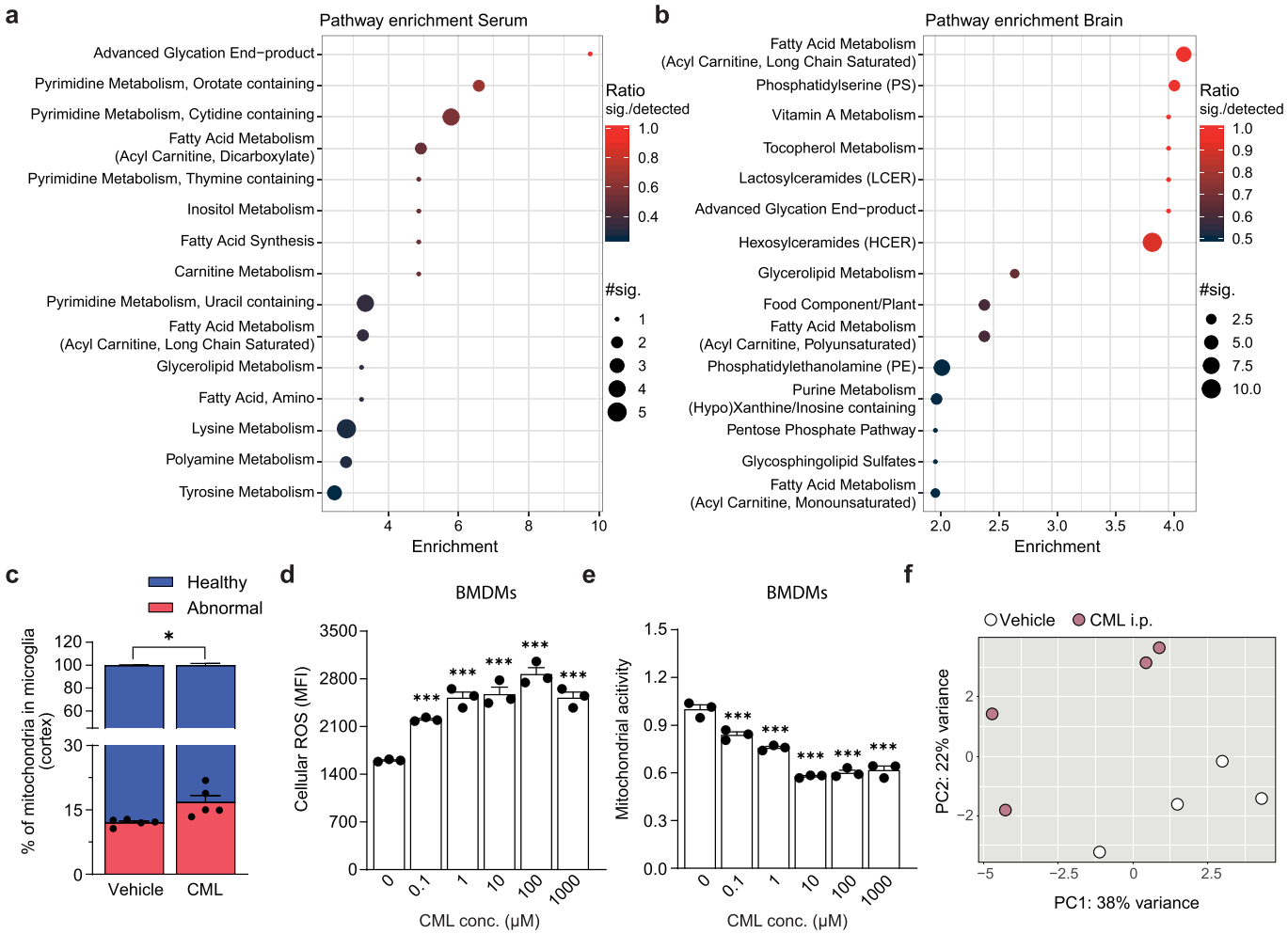

Extended Data Fig. 5 | CML modulates macrophage metabolism. (a, b) Pathway enrichment analysis for significantly abundant metabolites in serum and brain of aged mice (plotted are the top 15 enriched pathways). Color scale (blue to red), ratio between the number of significant metabolites to the total number of metabolites detected in each pathway. Dot size reflects number of significant metabolites in each pathway. Pathway enrichment analysis was performed automatically using the Metabolon's client portal. (c) Percentage of healthy vs abnormal mitochondria from total mitochondrial number in cortical microglia of young-adult mice treated with vehicle or CML i.p. (n = 5). (d and e) Bone marrow derived macrophages (BMDMs) were cultured in serum-free medium 6 h before the experiment. Cells were incubated with increasing concentrations of CML for 48 h, before harvesting for measurements. Each dot is a biological replicate (n = 3). (d) Quantification of relative MFI of CellROX probe signals. (e) Mitochondrial activity depicted as mitochondrial membrane potential ($\Delta\psi m$) (TMRM dye MFI) normalized to mitochondrial mass (MitoTracker Green MFI). (f) PCA on transcriptome (normalized gene counts) of microglia isolated from young-adult mice treated with vehicle or CML i.p.. (c-f) Data are presented as mean values + SEM. Each dot represents one mouse. Statistical analysis (c) two-way ANOVA followed by Sidak's multiple comparisons test, (d and e) one-way ANOVA followed by Dunnett's post-hoc test (***$p < 0.001$, ns = not significant). Exact p-values are reported in the source data.

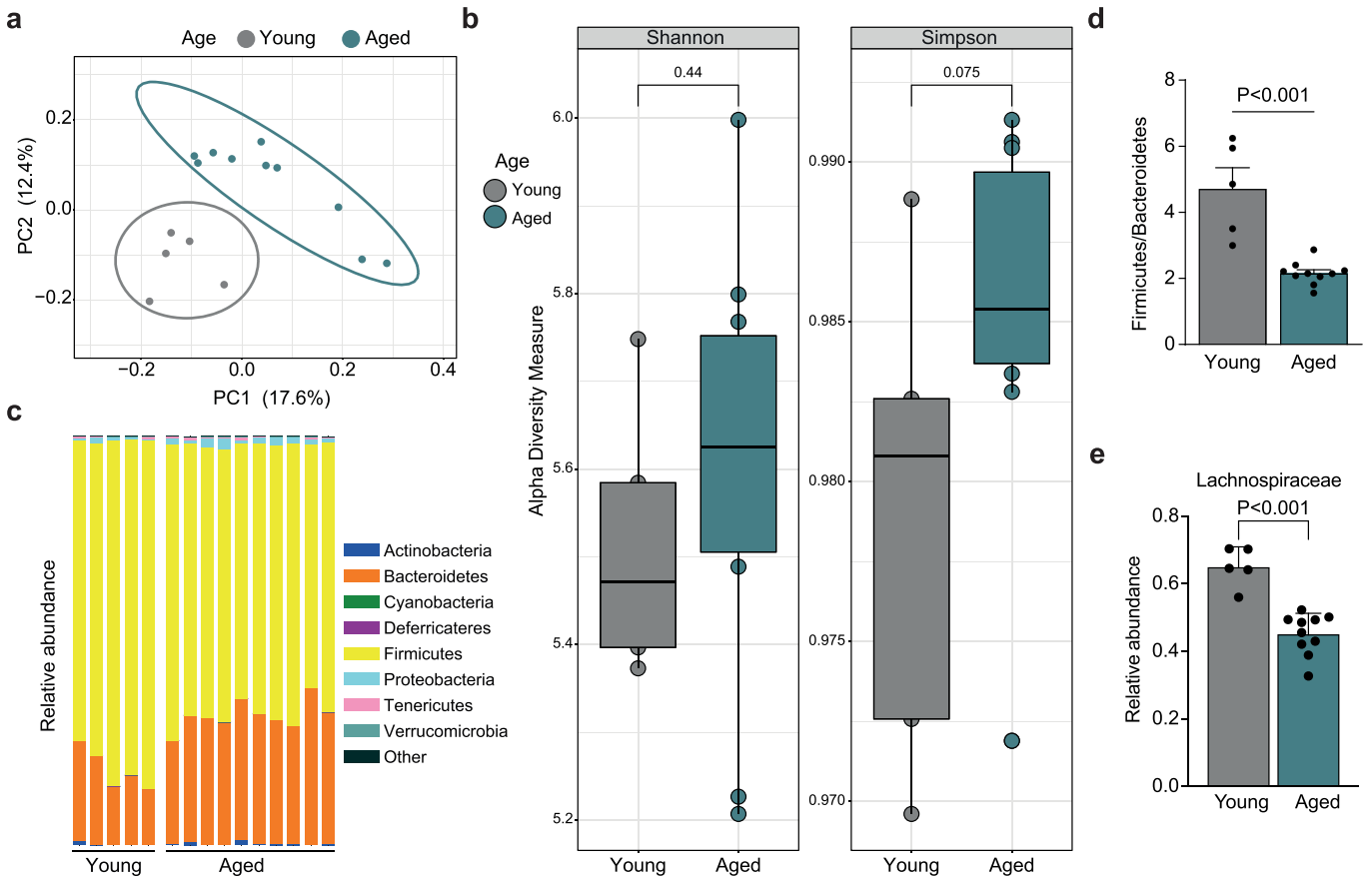

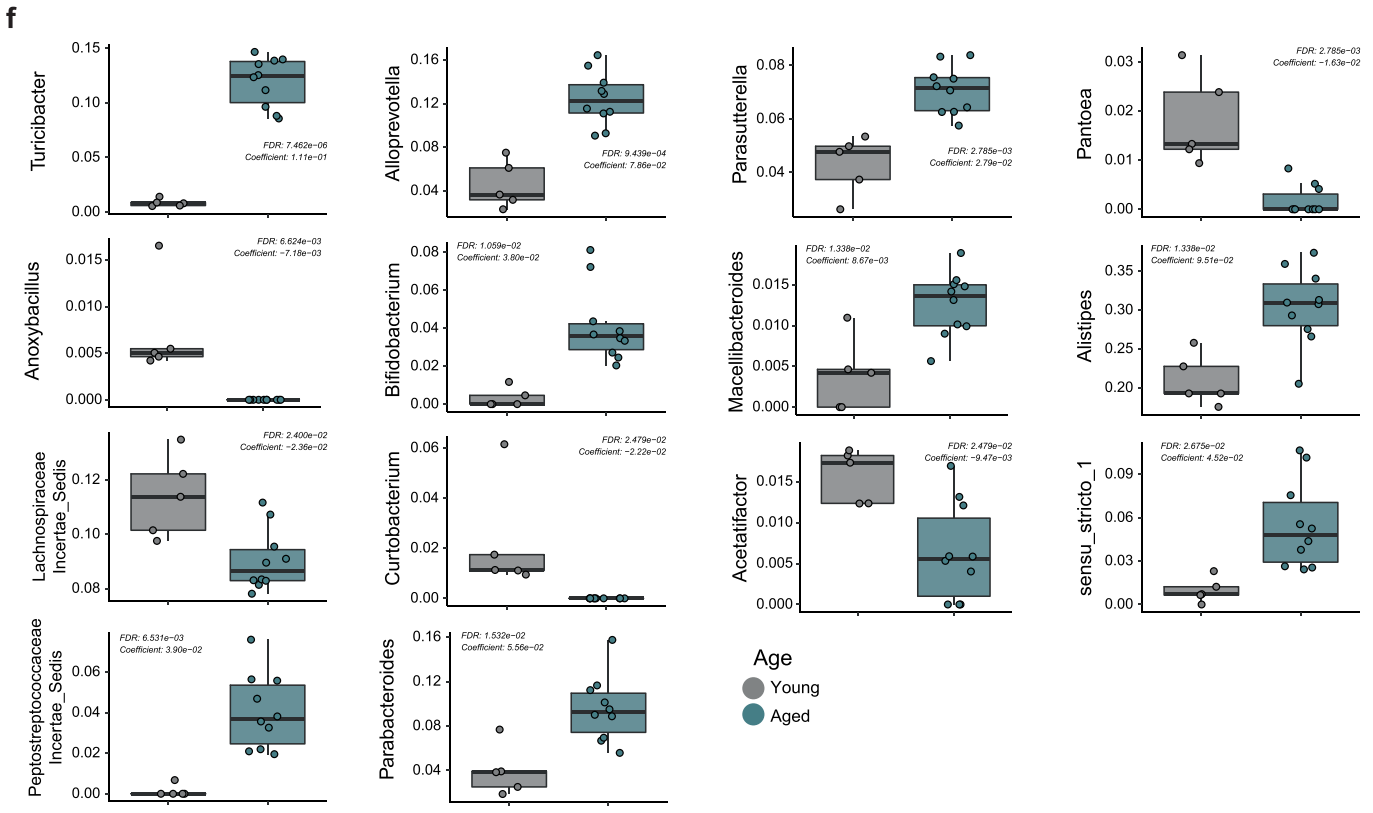

Extended Data Fig. 6 | See next page for caption.

Extended Data Fig. 6 | Age-dependent shift in gut microbiota composition. (a) PCA plot (beta-diversity) and (b) Shannon and Simpson alpha-diversity indices of gut microbiota. Non-parametric Mann-Whitney U-tests (two-sided) to compare alpha diversity between samples and Adonis from vegan package to assess the effects of groups for beta diversity. (c) Relative abundance of gut microbiota composition profiles at the phylum level in male mice at different ages (each color represents one bacterial phylum). (d) The average *Firmicutes/Bacteroidetes* ratio (F/R) in the cecal samples. (e) Relative abundance of the family *Lachnospiraceae*. (a-f) Data from young-adult and aged male mice, housed under SPF conditions (n = 5, 10). Each dot represents data from one animal. (d and e) Data are presented as mean values + SEM. (b and f) Box plots; centre = median, upper and lower "hinges" correspond to the first and third quartiles (the 25th and 75th percentiles), upper whisker extends from the hinge to the highest value that is within 1.5 * IQR of the hinge, and lower whisker extends from the hinge to the lowest value within 1.5 * IQR of the hinge, where IQR is the inter-quartile range, or distance between the first and third quartiles. (d and e) Statistics with Mann-Whitney U test (two-sided) (f) Relative abundance of differentially abundant genera in aging. Taxonomic differences at phylum and genus levels between tested groups were identified using the "multivariate analysis by linear models" (MaAsLin) R package.

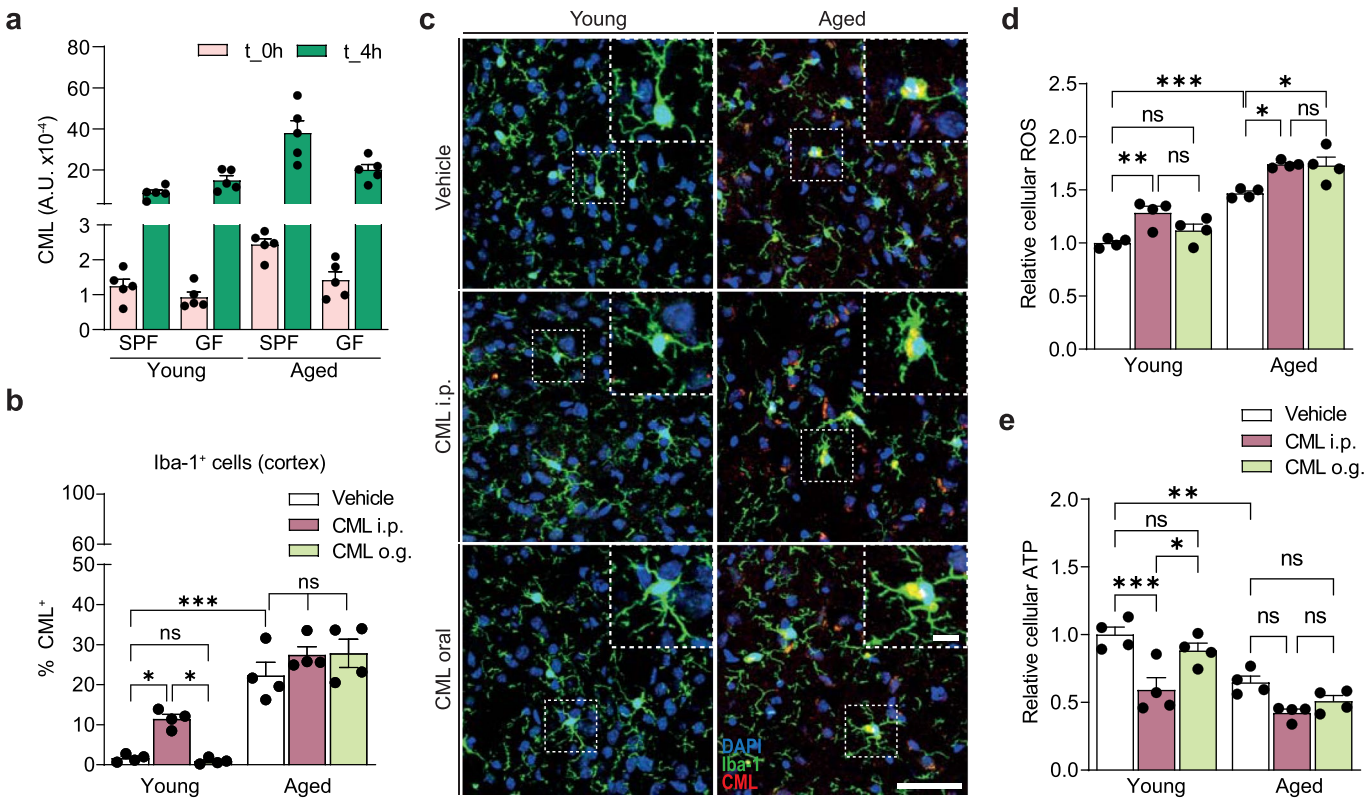

Extended Data Fig. 7 | Age-related microglial CML accumulation is gut-mediated. (a) Targeted metabolomics (LC/MS) on CML translocated into the circulation 4 h post oral gavage in young-adult and aged mice housed under SPF or GF (n = 5). Light purple; before gavage, green; 4 h post gavage. Each dot represents an individual measurement for one mouse. (b-e) Data from young-adult and aged SPF mice injected with vehicle or CML (i.p. or o.g.) (n = 4 each). Each dot represents one mouse. (b) Percentage of CML⁺ Iba-1⁺ cells quantified in the cortex. (c) Immunofluorescent labelling of CML (Red), Iba-1 (green) and DAPI (blue) in mouse cortex. Scale bars, 50 µm (overview) and 10 µm (inset). (d) Quantification of relative CellROX probe signal by determining MFI and (e) quantification of relative cellular ATP. (a, b, d and e) Each dot represents one mouse. Data are presented as mean values + SEM. Statistical analysis (b, d and e) two-way ANOVA followed by Tukey's post-hoc test (*$p < 0.05$, **$p < 0.01$, ***$p < 0.001$, ns = not significant). Exact p-values are reported in the source data.

nature research

Corresponding author(s): Dr. Thomas Blank

Last updated by author(s): Jan 26, 2022

Reporting Summary

Nature Research wishes to improve the reproducibility of the work that we publish. This form provides structure for consistency and transparency in reporting. For further information on Nature Research policies, see our Editorial Policies and the Editorial Policy Checklist.

Statistics

For all statistical analyses, confirm that the following items are present in the figure legend, table legend, main text, or Methods section.

n/a	Confirmed	
☐	☒	The exact sample size (*n*) for each experimental group/condition, given as a discrete number and unit of measurement
☐	☒	A statement on whether measurements were taken from distinct samples or whether the same sample was measured repeatedly
☐	☒	The statistical test(s) used AND whether they are one- or two-sided *Only common tests should be described solely by name; describe more complex techniques in the Methods section.*
☒	☐	A description of all covariates tested
☐	☒	A description of any assumptions or corrections, such as tests of normality and adjustment for multiple comparisons
☐	☒	A full description of the statistical parameters including central tendency (e.g. means) or other basic estimates (e.g. regression coefficient) AND variation (e.g. standard deviation) or associated estimates of uncertainty (e.g. confidence intervals)
☐	☒	For null hypothesis testing, the test statistic (e.g. *F*, *t*, *r*) with confidence intervals, effect sizes, degrees of freedom and *P* value noted *Give P values as exact values whenever suitable.*
☒	☐	For Bayesian analysis, information on the choice of priors and Markov chain Monte Carlo settings
☒	☐	For hierarchical and complex designs, identification of the appropriate level for tests and full reporting of outcomes
☐	☒	Estimates of effect sizes (e.g. Cohen's *d*, Pearson's *r*), indicating how they were calculated

Our web collection on statistics for biologists contains articles on many of the points above.

Software and code

Policy information about availability of computer code

Data collection	- Brightfield and flourescence microscopy: Images were acquired using BZ-9000 Biorevo microscope (Keyence) using 20x 0.75 NA objective, Olympus Fluoview 1000 confocal laser scanning microscope, or with a TCS SP8 X (Leica) using a 20x 0.75 NA objective (HC PL APO x20/0.75 NA IMM CORR CS2). -Electron microscopy: images were acquired with a 7,900x or 46,000x magnification using CM100 Electron Microscope (Philips). -Cell sorting for RT-qPCR and RNA-sequencing was performed on a MoFlo Astrios (Beckman Coulter, Krefeld, Germany). -Flow cytometric analyses were perfomed with the FACSCanto II (BD Bioscience, Heidelberg, Germany) and acquired with FACSDiva v6 software. -Non-targeted mass spectrometry (MS) analysis was performed at Metabolon, Inc., USA. -Targeted metabolite quantification by LC-MS was carried out using an Agilent 1290 Infinity II UHPLC in line with an Agilent 6495 QQQ-MS operating in MRM mode. Peak areas were identified based on standards for each metabolite and calculated using MassHunter (v B.08.02, Agilent). -16rRNA microbiome profiling was done using primers targeting the V5/V6 region of the 16S rRNA gene. Products were sequenced on an IonTorrent PGM system.
Data analysis	Graphpad Prism v9, ImageJ v1.53c, Photoshop CC 2019, Imaris v8.02, iTEM Software (Olympus), FlowJo v10.5.3, Microsoft Excel 2019, CASAVA v1.8.2, R v3.4 & v4.1.0, pheatmap v1.0.8, FastQC v0.67, Trim Galore! v0.4.3, STAR aligner v2.5.2, FeatureCount v1.5.3, Galaxy.eu, DESeq2 v1.32.0, WGCNA v1.69, goseq v1.44.0, ggplot2 v3.3.5, MassHunter vB.08.02.

For manuscripts utilizing custom algorithms or software that are central to the research but not yet described in published literature, software must be made available to editors and reviewers. We strongly encourage code deposition in a community repository (e.g. GitHub). See the Nature Research guidelines for submitting code & software for further information.

Data

Policy information about availability of data

All manuscripts must include a data availability statement. This statement should provide the following information, where applicable:

- Accession codes, unique identifiers, or web links for publicly available datasets
- A list of figures that have associated raw data
- A description of any restrictions on data availability

-Mouse genome version mm10 (UCSC; https://www.ncbi.nlm.nih.gov/assembly/GCF_000001635.20/).
-Lists of ROS-related genes were extracted from GO:0000302, GO:2000377, and oxidative stress; WikiPathways.
-Microglia RNA-seq data are available at (GEO accession number, GSE182719).
-Human metabolomics data were obtained from (https://www.nature.com/articles/ng.3809). Cohorts acquired through the TwinsUK databank (http://twinsuk.ac.uk/resources-for-researchers/access-our-data/). Data analyzed in this study are provided in extended supplementary tables.
-Raw data on serum and brain of young adult and aged mice groups were mined from (https://www.nature.com/articles/s43587-021-00141-4). Data analyzed in this study are provided in extended supplementary tables.
-Taxonomy assignment using Silva database (release 119) (www.arb-silva.de).
-Microbiome profiling (16S rRNA-seq) raw data are available at (https://doi.org/10.6084/m9.figshare.15179775.v1).

Field-specific reporting

Please select the one below that is the best fit for your research. If you are not sure, read the appropriate sections before making your selection.

☒ Life sciences ☐ Behavioural & social sciences ☐ Ecological, evolutionary & environmental sciences

For a reference copy of the document with all sections, see nature.com/documents/nr-reporting-summary-flat.pdf

Life sciences study design

All studies must disclose on these points even when the disclosure is negative.

Sample size	No statistical methods were used to pre-determine sample sizes but our sample sizes are similar to those reported in previous publications(doi:10.1016/j.cell.2017.11.042; doi:10.1038/s43587-021-00093-9; doi:10.1016/j.cmet.2021.10.010)
Data exclusions	Three samples were excluded from the RNA-seq analysis for not meeting the read quality thresholds.
Replication	All attempts at replication were successful.
Randomization	Wherever applicable, animals were randomly assigned to the different experimental groups. TwinsUK human data was a longitudinal time course. All data was considered without group allocation.
Blinding	The experimenters were blind with respect to group assignments.

Reporting for specific materials, systems and methods

We require information from authors about some types of materials, experimental systems and methods used in many studies. Here, indicate whether each material, system or method listed is relevant to your study. If you are not sure if a list item applies to your research, read the appropriate section before selecting a response.

Materials & experimental systems

n/a	Involved in the study
☐	☒ Antibodies
☒	☐ Eukaryotic cell lines
☒	☐ Palaeontology and archaeology
☐	☒ Animals and other organisms
☐	☒ Human research participants
☒	☐ Clinical data
☒	☐ Dual use research of concern

Methods

n/a	Involved in the study
☒	☐ ChIP-seq
☐	☒ Flow cytometry
☒	☐ MRI-based neuroimaging

Antibodies

Antibodies used	For histological analysis: Rabbit anti-Iba-1 Wako Cat# 01919741; RRID: AB_839504 Guinea pig anti-Iba1 Synaptic Systems Cat# 234004; RRID: AB_2493179 Biotinylated goat anti-rabbit Southern biotech Cat# 4030-08; RRID: AB_2795936

Rabbit Anti-Carboxymethyl Lysine antibody Abcam Cat# ab27684; RRID: AB_725920
Rabbit anti-iNOS Thermo Fisher Scientific Cat# PA3-030A; RRID: AB_2152737
Streptavidin-horseradish peroxidase (Southern Biotech) Cat# 7100-05
Alexa Flour 488-conjugated Donkey anti-Rat Thermo Fisher Scientific Cat# A21208; RRID: AB_2535794
Alexa Flour 568-conjugated Donkey anti-Mouse Thermo Fisher Scientific Cat# A10037; RRID: AB_2534013
Alexa Fluor 568 goat anti Guinea pig Thermo Fisher Scientific Cat# A11075; RRID: AB_2534119
Alexa Fluor 647-conjugated Donkey anti-Rabbit Thermo Fisher Scientific Cat# A31573; RRID: AB_2536183
Flow cytometry:
Biotinylated Rat anti-CD11b Thermo Fisher Scientific Cat# 13-0112-82; RRID: AB_466359
FC receptor blocking antibody CD16/CD32 BD Bioscience Cat# 564219; RRID: AB_2728082
Rat anti-mouse CD11b APC conjugated Thermo Fisher Scientific Cat# 17-0112-83; RRID: AB_469344
Rat anti-mouse CD11b BV421 conjugated Biolegend Cat# 101236; RRID: AB_11203704
Rat anti-mouse CD19 PE-Cy7 conjugated Biolegend Cat# 115520; RRID: AB_313655
Rat anti-mouse CD3 PE-Cy7 conjugated Biolegend Cat# 100219; RRID: AB_1732068
Rat anti-mouse CD45 PE conjugated Thermo Fisher Scientific Cat# 12-0451-83; RRID: AB_465669
Rat anti-mouse CD45 PE-Cy7 conjugated Thermo Fisher Scientific Cat# 25-0451-82; RRID: AB_2734986
Rat anti-mouse CD45R PE-Cy7 conjugated Biolegend Cat# 103222; RRID: AB_313005
Rat anti-mouse Ly6C PE-Cy7 conjugated BD Bioscience Cat# 560593; RRID: AB_1727557
Rat anti-mouse Ly6G PE-Cy7 conjugated BD Bioscience Cat# 560601; RRID: AB_1727562
Fixable viability dye eFluor 780 Thermo Fisher Scientific Cat# 65-0865-18
CellROX DeepRed Thermo Fisher Scientific Cat# C10422
Tetramethylrhodamine Methyl ester Perchlorate (TMRM) Thermo Fisher Scientific Cat# T668
MitoTracker Green FM Thermo Fisher Scientific Cat# M7514

Validation

Commercial antibodies were validated for the respective species by the manufactures as indicated on their websites. Choice was restricted to KO-validated antibodies or ones that are widely used in literature.

Animals and other organisms

Policy information about studies involving animals; ARRIVE guidelines recommended for reporting animal research

Laboratory animals	SPF and GF housed C57BL/6 mice were analyzed at (young adult) 6-10, and (aged) 96-104 weeks of age. Mice of the aged group in the non-targeted metabolomic analysis were 17-18 months old. Except for non-targeted metabolomics and microbiota profiling, where male mice were used, all groups comprised mice from both sexes. Mice were housed under a 12-h light, 12-h dark cycle and Temperatures of 18-23°C with 40-60% humidity, with food and water ad libitum. To avoid cage effects, mice from at least three different cages per experimental group were analyzed. For modulation of CML in aged animals, 18 months old SPF-housed C57BL/6 mice were used.
Wild animals	The study did not involve wild animals
Field-collected samples	The study did not involve animals collected from the field
Ethics oversight	All animal experiments were approved by local administration in Germany (Regierungspräsidium Freiburg) and were performed in accordance to the respective national, federal and institutional regulations and the guidelines of the Federation of European Laboratory Animal Science Associations.

Note that full information on the approval of the study protocol must also be provided in the manuscript.

Human research participants

Policy information about studies involving human research participants

Population characteristics	The TwinsUK adult twin registry includes about 14,000 subjects, predominantly females, with disease and lifestyle characteristic similar to the general UK population. Data from (Long et al., 2017) were 96.6% female in the age range 32 to 87 years (median 58 years).
Recruitment	Data were collected by the TwinsUK databank. Participants were recruited from the general UK population through national media campaigns. Other than the subjects being mostly females, no selection biases can be expected to impact results.
Ethics oversight	St. Thomas' Hospital Research Ethics Committee approved the studies, and all twins provided informed written consent.

Note that full information on the approval of the study protocol must also be provided in the manuscript.

Flow Cytometry

Plots

Confirm that:

☒ The axis labels state the marker and fluorochrome used (e.g. CD4-FITC).

☒ The axis scales are clearly visible. Include numbers along axes only for bottom left plot of group (a 'group' is an analysis of identical markers).

☒ All plots are contour plots with outliers or pseudocolor plots.

☒ A numerical value for number of cells or percentage (with statistics) is provided.

Methodology

Sample preparation	A detailed description of the sample preparation procedure is given in the Methods section "Flow cytometry".
Instrument	Cells were analyzed using BD FACSCanto™ II Flow Cytometer (BD Biosciences)
Software	Data were acquired with FACSDiva v6 (Becton Dickinson). Postacquisition analysis was performed using FlowJo v10.5.3.
Cell population abundance	For RNA-seq, 10,000 microglia were sorted per sample.
Gating strategy	Small debris was removed with the preliminary FSC/SSC gate. Single, living cells were obtained by doublet exclusion and exlusion of dead cells with Fixable Viability Dye eFluor® 780. Lineage exclusion was undergone by selecting population negative for CD3, CD19, Ly6C, Ly6G, CD45R. Microglia were gated on CD11b pos CD45 intermediate. for mitochondrial dyes, positive gatings were set using FMO controls.

☒ Tick this box to confirm that a figure exemplifying the gating strategy is provided in the Supplementary Information.